LASER INTERFEROMETER GRAVITATIONAL WAVE OBSERVATORY
- LIGO -
CALIFORNIA INSTITUTE OF TECHNOLOGY
MASSACHUSETTS INSTITUTE OF TECHNOLOGY

Technical Document LIGO-T970060-00 - D 18 Feb 1997

Alignment Sensing/Control Preliminary Design

Peter Fritschel, Gabriela Gonzalez, Daniel Sigg, Mike Zucker

Distribution of this draft:

ASC PDR Committee

This is an internal working note
of the LIGO Project.

California Institute of Technology
LIGO Project - MS 51-33
Pasadena CA 91125
Phone (818) 395-2129
Fax (818) 304-9834
E-mail: info@ligo.caltech.edu

Massachusetts Institute of Technology
LIGO Project - MS 20B-145
Cambridge, MA 01239
Phone (617) 253-4824
Fax (617) 253-7014
E-mail: info@ligo.mit.edu

WWW: http://www.ligo.caltech.edu/

1. OVERVIEW OF DESIGN STATUS

This document, taken with the supporting analysis documents given in the references (Appendix 3), describes the current ASC design. The design information in this document supersedes that in the ASC Conceptual Design Document. We summarize here the major design advances and changes since the conceptual design:

- Installation Support: the use of the 4km tube for establishing the initial beam axis has been included in the design; a more detailed sequencing for determining the initial optic orientations has been worked out; schemes for handling the effects of the optic wedges have been identified
- Lock Acquisition: extension of the (static) modal model to wide angles has given important information on the critical alignment degrees-of-freedom for lock acquisition; a possible scheme for a sequential ISC acquisition procedure has been identified
- Detection Mode alignment: advances and changes for the detection mode design are summarized in section 5.1.
- Diagnostics: Specific diagnostic tests, and electronics requirements for implementing them, have been defined.
- Test Plan: the major R&D project in support of the ASC – the Fixed-Mass Interferometer (FMI) – was successfully completed; a test setup and plan for prototype ASC hardware and software has been proposed and is being evaluated.

There are some areas of the design that we would prefer be further along at this stage:

- Installation Support: hardware designs for the specific alignment fixtures and tools have not been made.
- Optical Levers: a prototype optical lever was built and tested, but additional tests are needed.
- Lock Acquisition: the dynamic modal model incorporating a control system is still in development; until this model has been exercised - and supported with results from locking the 40m - the alignment tolerance for acquisition will remain an open issue.

The recent addition of a new mechanical engineer to the ISC group will speed the advancement of the first two items in the final design phase, and we expect that they will be appropriately developed at the Final Design Review. The third item relies on on-going model development; we have recently made a plan for testing and implementing the near-complete dynamic modal model code.

2. SUBSYSTEM INTERFACES

2.1. COS beam delivery

It is assumed that all designated interferometer output beams and sample beams originating in vacuum:

- are fully collimated (waist position to lie within 2 m^{TBR} of exit vacuum I/O port)

- have Gaussian beam radii 2 $\text{mm}^{TBR} < w < 4\ \text{mm}^{TBR}$
- exit vacuum I/O ports within +/- 5 cm^{TBR} of nominal IFO beam height
- exit I/O ports within 10 degrees^{TBR} of parallel to a horizontal ray perpendicular to the nominal IFO beam axis
- accumulate no wavefront aberrations exceeding $\lambda/10^{TBR}$ between the originating COC surface(s) and the exit interface

In order to facilitate the design of the ASC Guoy phase telescopes, the Guoy phase at a defined exit plane must be specified to within $5^{\circ TBR}$, or equivalently the specific COS beam reduction design must be supplied to the ASC; the tolerances in this design must be such that the Guoy phase at the exit port can be determined by calculation to within $5^{\circ TBR}$.

2.2. LSC

Because of the integrated nature of the LSC and ASC, there will be a more global ISC supervisory control function governing the lock acquisition sequence, diagnostics, and other common interferometer control signals.

2.3. SUSpensions

For ASC alignment control signals sent to the SUS controller, the following interfaces and specifications apply:

- ASC input to SUS controller is in the optic’s pitch-yaw basis (transformation to individual coil currents done in SUS controller
- Sensitivity of SUS input in radians/volt (vs. frequency if applicable): TBD
- Range: +/- 10^{-4} rad for $f >$ 10 mHz; +/- 1 mrad for $f <$ 10 mHz.

The following interfaces and specifications apply to the supervisory control of the local damping control:

- Damping mode control: ASC will have the capability of switching between the different modes of local damping (velocity damping; velocity damping with low frequency gain; no damping). Control interface type and specs: TBD.
- Input sensor control: ASC will have the capability of switching the sensor input for the local damping between the suspension sensors and the ASC optical levers
- ASC optical lever signals used for local damping will be interfaced to the SUS controller in the pitch/yaw basis; sensitivity of SUS input TBD.

SUS outputs sent to the ASC/ISC supervisory control:

- suspension sensor signals, in pitch/yaw units; rate and other specs TBD

The following interfaces and specifications apply to the ASC orientation readout function for the SUS installation:

- readout format: TBD (digital meter, e.g.)

- update rate: TBD

2.4. SEI control operation

To compensate for long term alignment drifts (due probably to stack drifts), SEI will provide off-line control inputs for translating the stack transverse to the optic axis (for long term beam centering control) and for rotating the stack about the vertical (for long term optic yaw control). The ranges of these actuators are given in the SEI DRD. Specifications for the control inputs are TBD.

2.5. IOO control operation

The ASC design for the mode cleaner (MC) alignment calls for control inputs for the direction of the MC input beam, in the basis of input beam angle and position (reference plane at the MC waist). Specifications for these inputs are TBD.

3. INITIAL ALIGNMENT - INSTALLATION SUPPORT

3.1. Changes from the conceptual design

The installation support design has been modified in several key respects:

- The design of IO alignment and installation support for IO are now part of ASC scope; while some requirements associated with IO are still TBD (e.g., MC length precision, centering requirements on telescope mirrors and Faraday isolator) we feel it is likely these specifications will be accommodated by the general plan outlined here.
- Axial positioning of optics is likely to become part of ASC scope (though this is currently not official). Requirements for the precision of this positioning are TBD; in anticipation, we have outlined a baseline proposal involving standard measuring tools, capable of a few mm accuracy over the station.
- Dead reckoning of the beam tube centerline from facility station monuments alone was judged too unreliable given the results of the Hanford beam tube slab survey. Despite the potential schedule impact (TBD), we now plan to open the gate valves under vacuum and sight the far end from each station to establish a pilot beam parallel to the beam tube axis.
- The use of DMT's (Dummy Mirror Tools) to transfer the pilot beam normal to the optical lever system was principally motivated by a desire to decouple the ASC setup work from the suspension installation. It is not clear that this schedule decoupling is actually needed, and the use of the intermediate transfer standard introduced additional opportunities for error. As a result, our baseline plan is now to use the pilot beam system directly on each suspended optic during its installation. We may still prepare a DMT as a backup (for instance, if a suspension is held up for some reason). We also retained one (but called it something less silly) for installation of the beamsplitter; see 3.4.2.
- Pilot beams are now to be generated by laser autocollimators rather than simple laser transits, and the lateral transfer of their beam to the mirror axis will be accomplished (in most instances) by hollow retrorereflectors rather than periscopes. Use of the autocollimation feature permits higher precision in setting the optic normal to the pilot beam than the beam over-

lap method previously proposed.

- To facilitate transverse centering of suspended optics on the various offset positions required in the corner station, transparent measurement reticles combined with a video caliper measurement unit will be used in conjunction with a CAD-based positioning database. This should be faster and more accurate, and should reduce the amount of human access required inside the chambers.

3.2. Installation support functions & requirements

Suspended core optics and some suspended input optics will have restricted ranges of adjustment after installation. For example, the COC suspension will permit no more than +/- 1 milliradians of pitch or yaw adjustment (SUS DRD). In addition, RF sideband resonance conditions constrain the ratio between the mode cleaner and recycling cavity length (LIGO-T960122), and alignment thermal noise requires accurate centering of the resonant mode on the physical center of each core optic (ASC DRD). It is therefore necessary to establish accurate fiducial positions and equilibrium angles for these optics, referenced to the site coordinate system, at the time of their installation. ASC will provide the procedures and tooling to measure and verify these translations and angles, and the means to evaluate or restore them after disturbances (including, for example, pumpdown).

Transverse position settings must be +/- 1 mm or better for input test masses, +/- 5 mm or better for beamsplitters, recycling mirrors and folding mirrors, and +/- 3 mm or better for mode cleaner mirrors (ASC DRD, T952007). Requirements on the axial position setting accuracy (for all optics) and on the transverse position accuracy of the IO beam expander components remain TBD at this time; for the purposes of this preliminary design, they are assumed to be no more stringent than +/- 3 mm for each. In general this permits setting the suspensions using standard surveying instruments placed outside the chambers.

Should tighter axial position precision be required, several alternate strategies have been proposed. One candidate under consideration uses a picosecond pulsed solid-state laser directed along the optical axis with high-speed detectors and precision timing equipment to make a sub-millimeter-resolution optical time domain reflectometer. Of course, this would be significantly more costly and require additional laboratory development. Convergence of axial position specifications and development of a consistent implementation will receive a high priority in the final design phase.

For all core optics and the final IO steering mirror, the goal for initial setting of the surface normal will be within +/- 50 microradians of the ideal optical axis (note that a beam reflected from such an optic will thus be within 100 microradians of the ideal direction). While the requirement (ASC DRD, T952007) is to use 10% or less of the suspension actuator dynamic range (i.e., +/- 100 microradians), achieving this more stringent goal will guarantee that reflected beams can be returned within the 1 meter clear aperture at 4 km, which will simplify subsequent alignment processes.

3.3. Facility monuments and initialization

LIGO Civil Construction will provide each LVEA/VEA station with alignment monuments ("brass plugs") bonded to the facility technical foundation. Approximately 12 monuments will be provided in the Hanford LVEA, 10 in the Livingston LVEA, and 6 in each end- or mid-station VEA. They are generally placed approximately one meter from the vacuum envelope at strategic points, chosen by PSI (the vacuum equipment contractor) to be near critical flanges in the vacuum system. These monuments are used by PSI to install the vacuum envelope; final chamber positions may deviate by no more than +/- 2.5 mm transverse to and +/- 25 mm parallel to the local laser beam axis with respect to ideal positions indicated by the monuments. However, the placement of these monuments and their relationship to the beam tube axes (marked by an independent set of references along the beam tube slab) remains LIGO's responsibility.

Figure 1: Example station plug layout (right end station; from 12/11/96 PSI proposal)

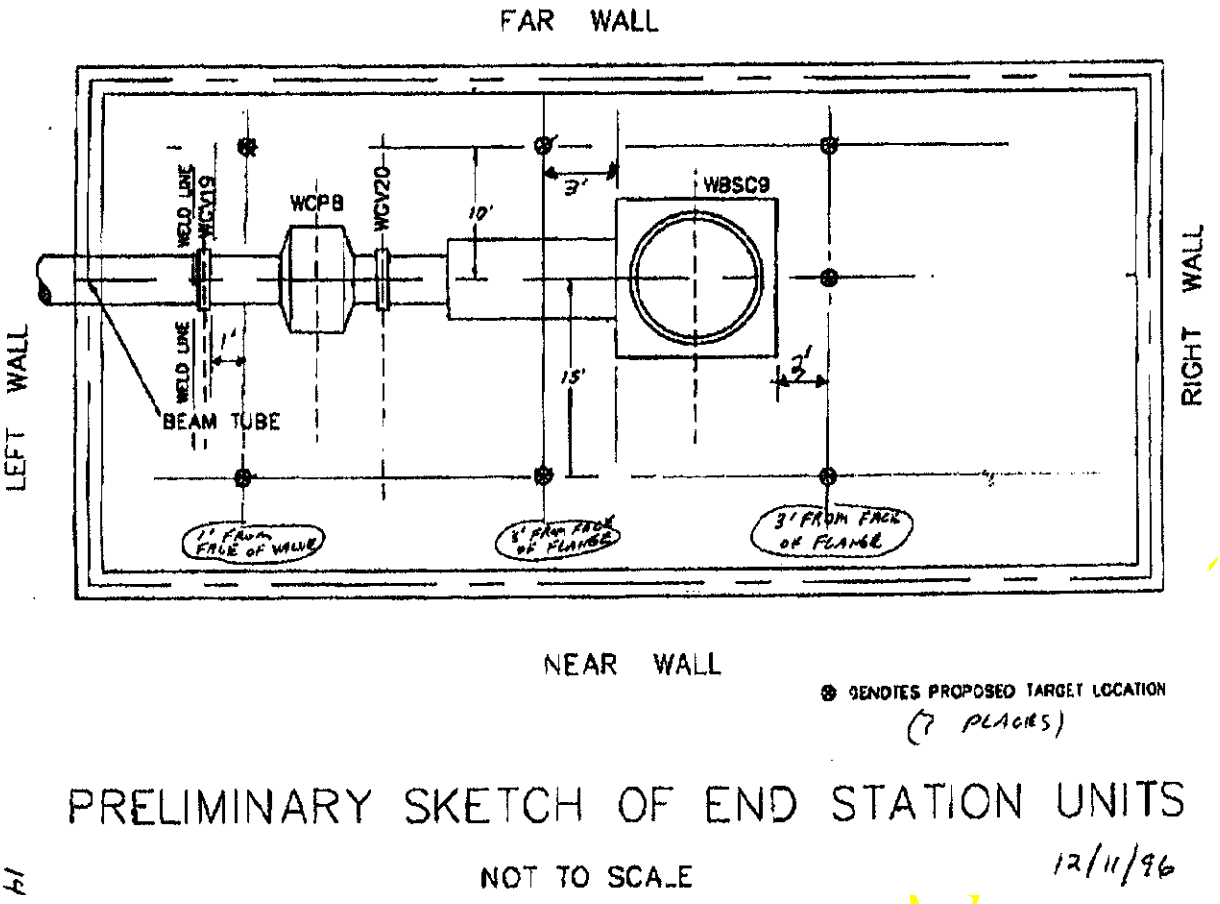

In principle, achieving absolute angular alignment with respect to the beam tube axes “blind” (i.e. from survey of pre-installed monuments alone) is advantageous from the standpoint of installation scheduling and risk management. For example, this would permit the detector installation to proceed essentially independent of the status of the beam tube modules (some of which may be undergoing bakeout at the appropriate time) and vacuum equipment (which might need to be vented at the appropriate time to serve other installation needs). This requires the ensemble of monuments in any given station to be angularly oriented to the beam tubes within a fraction of the +/- 50 microradian setup tolerance goal. This in turn would require knowing *differential* lateral and vertical offsets of successive plugs within a given station to better than +/-0.5 mm (the absolute common offset is not so critical). Unfortunately, analysis of the Hanford beam tube slab survey (LIGO-T960176) indicates that the best differential accuracy achieved there between adjacent monuments is of order 4 to 10 times worse than this. As a result, while all practical efforts should be taken to achieve the requisite precision in setting the station plugs, we do not feel secure in relying on sub-50 microrad alignment of the pattern to the tube axes.

Our alternate strategy involves direct sighting of the mid- or end-station through each evacuated beam tube, at a time when both station vacuum sections and the intervening beam tube module(s) are simultaneously under high vacuum. This will permit calibration of a semi-permanent alignment reference in each station which is parallel to the true tube axes.

ASC will furnish viewports for installation on the vacuum equipment, either prior to commissioning or shortly after LIGO acceptance (for example, at the same time that electrical feedthroughs are installed, permitting concurrent leak testing). At least one of these ports in each station will be installed on a nozzle affording a direct view of the beam tube clear aperture, at nominal height between 10 and 35 cm above the beam tube centerline. In the midstations at Hanford, where no such direct-view ports exist, vacuum-compatible periscopes (cf. Figure 13, Optical Lever Periscope) will be installed in selected nozzles on the manifold reducers A-1 and A-14 to give an equivalent internal view (see PSI V049-5-004). A laser autocollimator with visual reticle and electronic readout (e.g., Newport LAE500) on a kinematic platform is then mounted to the technical foundation in each station to obtain a clear view of the tube aperture through each of these ports. A total of six such units are needed at Hanford and four at Livingston; one is placed at each endstation or midstation (looking toward the corner station), and one looks down each beam tube from the corner stations. These units have specified resolution of 0.1 arcsecond (0.5 microradian), so the accuracy of the final installation will be limited by the stability of the supports (see 3.4.1.)

Two or more additional viewports will be installed on nozzles affording an interior view of the BSC chamber, HAM endcap, or (closed) isolation valve gate. A video camera mounted to one such port will image the chamber interior to detect transmission of the laser beam from the autocollimator at the far end. The other port will support a high-intensity illuminator (either a lamp or a collimated visible laser) to illuminate a spot on the chamber interior or valve gate which is visible through the clear aperture.

When all sections are at high vacuum, the isolation valves are opened and the chamber illuminators are turned on. Each autocollimator is adjusted to bring the image of the distant illuminated spot to the center of the reticle. Then, the interior chamber illuminators are turned off and the autocollimators' coaxial lasers are turned on; using the video imaging equipment, the centroid of the transmitted laser spot (which may be as much as 50 cm in diameter, depending on collimator and laser specifications) is brought to the center of the clear aperture at the far end. At this time the autocollimator adjustments are locked. The isolation gate valves may now be reclosed and the vacuum section backfilled.

3.4. Core Optics installation support

3.4.1. End- and Mid-station core optics

Only ETM's are contained in the end- and mid-stations. To prepare for installation, optical lever transmitter and receiver platforms are installed near the appropriate BSC or manifold viewport nozzles. After the local seismic isolation stack has been installed in the BSC and has settled to remove initial drift (drift period TBD pending measurements on prototype springs), a standard transit level and steel tape measure are used to determine the correct offset for the test mass suspension from the brass plugs, using their tabulated offsets. These marks are transferred to transits on tripods adjacent to the removable 60" doors on the BSC; the softwall cleanroom is craned into position, the chamber prepared for opening and the 60" doors removed. The optical lever and cavity transmission QPD viewports may now be installed on their nozzles, and the optical lever transmitter and receiver installed and connected. If needed, internal relay periscopes (Figure 13) are also installed at this time to bring the optical lever receiver beam and cavity transmission beam out.

Figure 2: End station core optic installation tooling arrangement

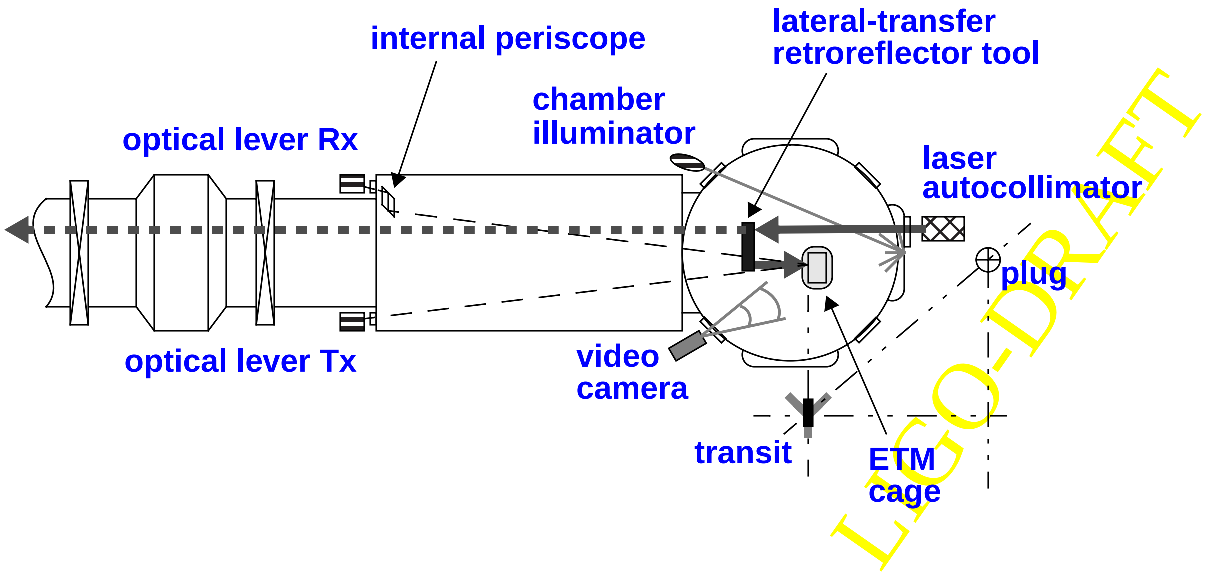

The stack mounting interface height and level are adjusted using external adjustment screws as indicated by the transit and a precision bubble level. Inside the chamber, vacuum-compatible translation stops (provided by others) are then bolted to the isolation stack mounting surface such that, when the suspension is installed against these stops, the optic will lie in the proper plane at the correct lateral and vertical offset from the beam tube centerline. Next, a lateral transfer retroreflector tool (Figure 3) is temporarily mounted to the stack interface facing the HR side of the suspended ETM, to intercept the autocollimator beam and redirect it backward toward the ETM face. This tool is noncontaminating, but need not be vacuum-compatible as it will be removed.

When the ETM itself is ready to be installed, the suspension crew proceeds by aligning the suspension cage to its position stops, rotating it in azimuth and adjusting the equilibrium pitch of the optic (using the suspension control bias) to retroreflect the autocollimator beam.

The optical lever laser is directed onto the ETM, and the reflected beam is nulled on its quadrant detector. Optical lever settings are then logged for reference. Finally, the transmitted autocollimator beam is used to align the cavity transmission beam reducer and center the transmission monitor QPD on the cavity axis (and thus the optical center of the ETM). This final step is noncritical since the monitor will be calibrated later by the operational beam centering procedure (see Section 7). At this stage the tool can be removed from the chamber and the chamber resealed.

Errors in the final alignment of the suspended optic may arise in several ways:

- A thermal gradient of 0.5 degree C across a simple steel support column 2 m high and 20 cm in diameter can induce an angle change of 50 microradians. If necessary, such deflections will be mitigated by thermal insulation and choice of low-expansion materials.
- Turbulence and heat flow in the air column between the autocollimator output and the viewport will induce random variations in the apparent reference direction. The air path will thus be enclosed and sealed, and sources of heat (including the autocollimator laser's heat sink and power supply) will be stabilized and/or insulated.
- The wedge of air inside the autocollimator's viewport will refract the beam differently between atmospheric pressure and vacuum, changing its angle by approximately one part in 10^4 of the nominal angle of incidence. To avoid a significant effect the beam should enter the viewport within about 10 degrees of normal. Where no available flange permits this, it may be necessary to provide an angled nozzle extension, or (since the effect is calculable) preemptively offset the autocollimator by the required amount.
- A less predictable vacuum-related effect is the distortion of the local technical foundation due to unbalanced air pressure on the chambers. An anchored BSC chamber resisting an unbalanced vacuum load will induce a local tilt of approximately 100 microradians (D. Coyne). In the above procedure, after pointing the autocollimator beam through the beam tube under vacuum, that tilt will be relieved when the chamber is backfilled to install the test mass. We will thus equip each autocollimator platform with a precision tiltmeter. This will be used to measure the pumpout tilt, which will be initially uncertain due to variability of the concrete, soil and boundary conditions. The tiltmeter signal may either be subtracted as an offset or nulled by readjustment of the platform. Since the shift is comparable in magnitude to the target accu-

racy, highly accurate cancellation is not necessary. (Note that the pitch of the single-loop suspension is determined gravitationally, so the slab deflection should not affect the mirror's equilibrium pitch. This compensation is thus only needed during suspension installation.)

Figure 3: Lateral transfer retroreflector arrangement

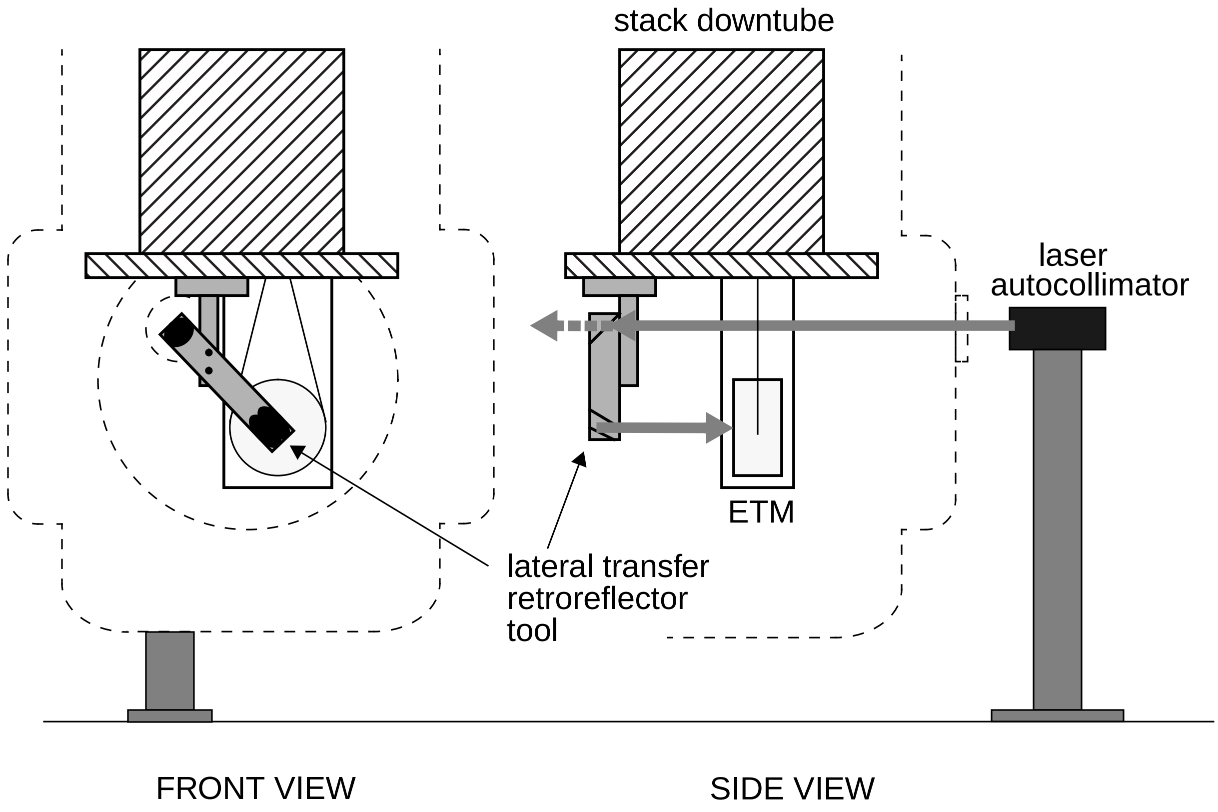

3.4.2. Corner station core optics

In the corner station, a similar procedure is employed to set each of the core optics, with some variations related to the number of optics and the need for accurate relative positioning between members of the group. The deflection of beams due to transmission through wedged substrates (wedges between 0.5 and 2 degrees, TBD) causes the recycling mirror, beamsplitter and IO beam expander output mirror to lie at different positions and angles with respect to the nominal cavity axis. These positions will be tabulated for each optic from the CAD optical layout; these tables may need to be updated with component test data (actual measured wedge and orientation, for example) to achieve sufficient accuracy.

For axial positioning, a pretensioned steel survey tape will be installed on the technical foundation parallel to each beam line and initially calibrated to the brass plugs by use of a transit and plumb bob. This has the advantage that it will not need to be repositioned and recalibrated when the softwall cleanrooms are moved from chamber to chamber. Axial positions will be transferred from this tape to a tripod-mounted right-angle laser sheet generator (e.g., White ML-200 or LaserTools L100LK) standing above it and adjacent to an open chamber access door; the projected laser sheet will then be used to set axial suspension cage positioning stops on the isolation stack, as for the end- and mid-stations.

To minimize the work of individually surveying the multiple lateral and vertical suspension offsets, jigs will be used to generate positions from the single autocollimator beam threading all the chambers of a given section. The jigs will consist of rigid aluminum frames with CNC-ruled Mylar reticles; the edge of each frame will be provided with kinematic mounting provisions to clamp to a SOS or LOS suspension cage. A commercial video caliper system, imaging these reticles from outside the chamber, will then be used to determine the offset of the mounting plane (and thus the optic center) from the centroid of the reticle-scattered autocollimator beam. The suspension installation team can then use the video caliper readout to install and lock down each cage.

ITM angles will be measured and set exactly as for ETM's; the autocollimator pilot beam (previously set parallel to the beam tube axis by sighting the far end) is intercepted by a lateral-transfer retroreflector and directed to the reflecting face of the ITM, which is rotated to achieve perfect retroreflection. The optical levers are then nulled for reference.

The beamsplitter, recycling mirror and folding mirrors (for the 2km interferometer) are not normal to the beam tube axis (in the case of the RM, it is because of the substrate wedges on the ITM and BS). Several options are available for dealing with this;

- After both ITM installations, their transmitted autocollimator beams follow approximately the same paths as the interferometer beam will. Installing the folding mirrors (WA 2k), beamsplitter, recycling mirror and IO beam expander output mirror in that order, the retroreflected beam passed backward through the entire chain will give (approximately) the correct angles for each optic. Temporarily offsetting the ITM by a known angle prevents confusion when setting the BS and RM angles. Because of the wavelength difference in substrate refractive index between IR and the visible (~ 635 - 670 nm is used in most commercial autocollimators), the visible beam is refracted by about 130 microradians more per degree of wedge, and a small compensation needs to be applied to each optic; the optical lever can provide a calibrated way to introduce this offset. Alternatively, the autocollimator could be modified to use a Nd:YAG laser or a diode laser at a nearby wavelength.
- One potentially inconvenient feature of this method may be that it relies on a specific installation sequence ("backward" from the ITM's to the IO beam expander). An arbitrary sequence can be followed if the lateral transfer retroreflector can be set up adjacent to the optic being installed. The local tilt of the beam (tabulated in advance from specifications or measurements of the intervening substrates) can be "dialed in" using a variable wedge plate, which is preset off-line to each required deviation angle and set between the suspension and the retroreflector.

Since autocollimation is not directly possible for the beamsplitter, an additional temporary optic is required to establish its angle (for either of the above general methods). A flat mirror on a kinematic adjustable mount is placed at side of the beamsplitter nearest the recycling mirror, and (using a lateral transfer retroreflector and the adjacent pilot beam) it is arranged normal to the beam axis and locked. The pilot beam from the other arm is then also retroreflected and bounced off the beamsplitter, onto this temporary mirror and back; as can be seen from Figure 4, when the beam returns to its source the cavity axes are properly reflected onto each other by the beamsplitter. The retroreflectors and temporary mirror are then removed.

Figure 4: Beamsplitter alignment using both corner station autocollimators.

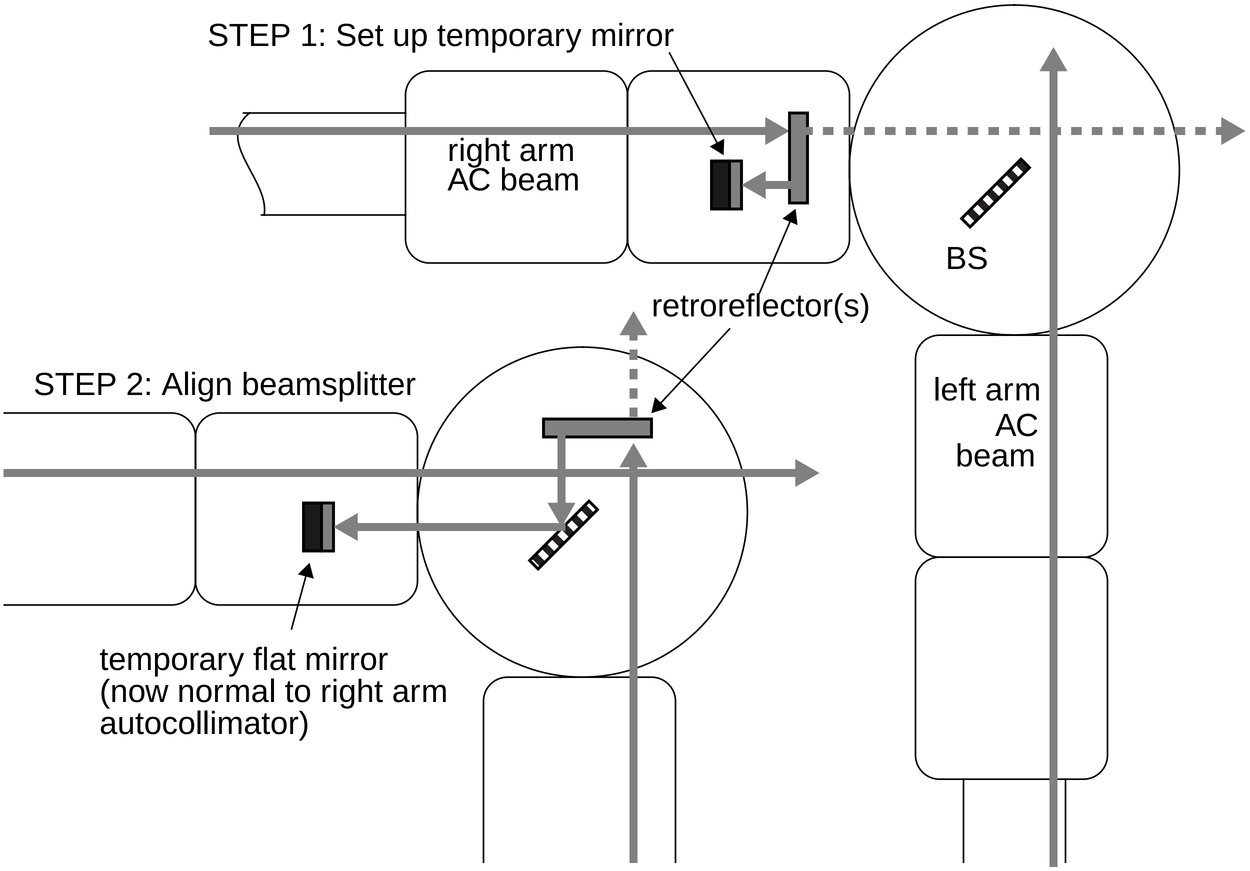

3.4.3. Input Optics installation support

The large final output steering mirror of the IO beam expanding telescope will be aligned along with the core optics, using the same methods and support equipment. However, all the small-diameter in-vacuum optics will be aligned as a group, decoupled from the large optics installation. This is useful because the input optics and laser must be commissioned and characterized very early in the installation sequence, and because their alignment and centering tolerances are generally less stringent. The adjustment afforded by the final two steering mirrors permits IO “absolute” alignment to deviate from the global coordinate system, up to limits determined by beam centering and baffle clearances.

A pilot beam system will still be used to derive the vertical and lateral component offsets (with Mylar reticles and a video caliper readout), although this pilot beam does not need to be completely parallel to the beam tube axes. If the main autocollimator beam is available at the time required it will be used; otherwise, another beam will be generated (e.g., from a commercial laser transit level) and set parallel to the mode cleaner tube. Precise axial positioning of the mode cleaner and telescope mirrors will be done in the same way as for the core optics.

The current baseline IO design (IO conceptual design document) is entirely reflective, except for two substrate transmissions in the mode cleaner input and output couplers (which cancel to lowest order) and the Faraday isolator. Thus it will be possible to achieve adequate alignment by sending a parallel beam backwards through the entire chain and adjusting each component in turn; this beam can be generated by a retroreflector placed at the output, or can be a separate laser beam. Finally, IO is making provision for operating the mode cleaner at low IR laser power in air, which will allow final adjustment of the cavity with the actual resonant mode before fully committing to the suspension positions.

4. ISC ACQUISITION PROCEDURE

4.1. Advances and Changes

Interferometer lock acquisition remains one of the major open issues for the ASC (how well does the interferometer have to be aligned before it can be locked?). A recent advance is the definition of an ‘idealized’ LSC acquisition procedure, where the interferometer lengths are sequentially brought into resonance (by ‘idealized’ we mean the fact that it assumes a perfectly aligned interferometer at each stage). In the context of this LSC procedure, we have tried to identify an alignment procedure that should allow the length locking to proceed as envisioned. The acquisition procedure outlined below is thus more of a combined LSC & ASC (i.e., ISC) acquisition procedure than presented at the DRR.

4.2. Wide angle modeling

Modal model simulations extended to many modes and applied at large angular misalignment are described in [T960191-00-D, update 5]. Three main topic were investigated: the modal decomposition of the electric fields, the servo-stability of the length sensing signals and the linearity of the wavefront sensing signals when the interferometer is close to resonance. The investigations were made along the axes which are diagonal for the degradation of the gravitational-wave readout: u_1 to u_5 as defined in Appendix 1. Table 1 summarizes the findings. Even though the angles for which the power in the recycling and the in-line arm cavity has dropped by factor of two and the stability boundaries for longitudinal and angular misalignment are vastly different in different directions, they are usually very similar in absolute values for each direction. The smallest limit for a stable alignment is obtained for a misalignment in the direction of $u_1 \sim 1\times10^{-7}$ rad. This misalignment involves only the recycling mirror and the ITMs, hence, suggesting that during lock acquisition the recycling cavity should be aligned before the arm cavities are brought into resonance.

Table 1 Power degradation and decrease of servo stability due to large angular misalignments. For each principle angular direction the angle for which the power has degraded by half and the angle for which the length and alignment sensitivities have decreased by half are shown. The values are given in units of the arm cavity divergence angle which is ~10^{-5} rad.

Direction	$\frac{1}{2}$ *Recycling cavity power*		$\frac{1}{2}$ *Arm power*	*Stability (half gain point)*	
	sidebands	*carrier*	*carrier*	*LSC*	*ASC*
u_5	> 1	> 1	> 1	> 1	> 1
u_4	0.7	0.6	0.5	0.6	0.65
u_3	0.3	> 0.6	> 0.6	0.15	0.15
u_2	0.15	0.06	0.06	0.04	0.04
u_1	0.015	> 0.1	> 0.1	~0.01	~0.01

4.3. Sub-states of the IFO

We use the following definitions of interferometer substates, where the state number corresponds to the number of length degrees-of-freedom that are resonant:

- **State 2:** The recycling cavity is resonant for the main sidebands, and the Michelson is at the point of zero path length difference for the carrier (normal dark port condition, even though there is very little carrier in the recycling cavity); carrier is nowhere resonant
- **State 3:** The conditions of state 2 hold, plus one of the arm cavities is resonant for the carrier
- **State 4:** The entire interferometer is resonant in the normal Detection Mode state.

4.3.1. Unlocked recycled Michelson - manual alignment

The recycled Michelson must be aligned well enough so that it can be locked in length. The first step will be to manually align the cavity consisting of the recycling mirror, the beamsplitter, and the on-line ITM (refer to Fig. 5a); the off-line ITM is given a large misalignment (the ETMs are also misaligned). The effect of the beamsplitter angles is insignificant, and this can be thought of as a (very lossy) two mirror cavity. An initial, relatively crude, alignment of this configuration is made by monitoring the video camera images of the spot patterns on the recycling mirror and on-line ITM, and collapsing the pattern to a ‘single spot’ by manually adjusting the mirror angles. The cavity length is then swept through several lambda by driving the RM, at a frequency of ~5 Hz. The power in the cavity is simultaneously monitored using the AR surface (ghost) beam from the ITM (using the dc readout of either an LSC photodetector or ASC wavefront sensor). The fringe contrast is then maximized by manually adjusting the pitch and yaw angles of the RM and ITM. This is done with the modulation index turned down (Γ~0.1 - enough to keep the mode cleaner locked) so there is no confusion from the different resonant lengths for the carrier and sidebands.

The maximum fringe contrast achievable in this configuration is 80%. Once something close to this is achieved, the off-line ITM is manually brought into alignment, so that its reflection interferes at the beamsplitter with the main beam (Fig. 5b). The off-line ITM alignment is optimized by monitoring the anti-symmetric port beam with a video camera (spatial interference fringes will be seen and will indicate the direction of misalignment), and the cavity power with the ITM ghost beam. The RM axial position is also driven in this phase, and the position of one of the ITMs may also be driven.

Once the power buildup in the recycling cavity is at least ~10% of the maximum possible level, the two length control loops are closed. The maximum possible level, as measured by the ITM ghost beam detector, can be inferred from the signal level measured in the first step (paragraph) above and the mirror transmissions.

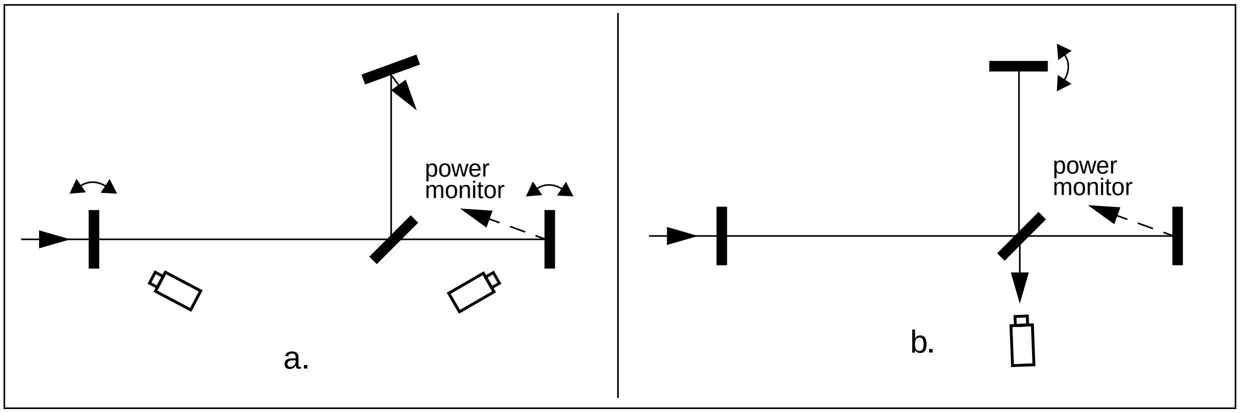

Figure 5 Steps involved in the manual alignment of the recycled Michelson. In step **a,** one of the ITM's is intentionally misaligned, and the other ITM and the RM are manually aligned using the spot patterns on these mirrors. In step b, the other ITM is then aligned, using the spot pattern at the anti-symmetric port for guidance.

4.3.2. Resonant recycled Michelson (state 2)

Once the recycled Michelson is locked in length by the LSC, the ASC will use the wavefront sensor system to further optimize its alignment. Because of the degeneracy of the recycling cavity, only two degrees-of-freedom can be aligned using the wavefront sensor signals - these are the ITM differential alignment, and the combination of recycling mirror and ITM common mode alignment corresponding to the eigenvector u_1 (refer to Appendix 1 or to ref. [4]).

The wavefront sensor signals 2a and 2b (coming from the I &Q phases of a single head at the reflection port) detect the same angle combinations as in Detection mode, the only difference being that in State 2 the signal strength (W/rad) is roughly 3× larger than in Detection mode. We thus can close the loops on these two degrees-of-freedom using the same transformation matrix as in Detection mode, using the acquisition servo loop described in section 5.4.2. We expect to be able to control these d.o.f. to 10^{-8} $\mathrm{rad}_{\mathrm{rms}}$ or better.

The on- and off-line beams are then centered on the two ETM transmission quadrant monitors. For the initial alignment, this will begin by getting the beams into the ETM stations, as described in sections 2.2.3 and 2.2.4 of the ASC Conceptual Design. The arm carrying the on-line beam will be monitored first. The input beam direction will be varied (using the IOO telescope mirrors) until the beam is detected in the on-line arm ETM chamber with that chamber's video camera (viewing the chamber interior). The beam is then manually directed to hit the ETM. The beam transmitted by the ETM is now picked up by the transmission quadrant monitor, and the beam can be centered on this monitor. The same procedure is then applied to the off-line beam, the only difference being that the beamsplitter angles are adjusted to direct the beam in the off-line arm.

Just before transitioning to State 3, the wavefront sensor servos will be disengaged so that they do not have to deal with the transients involved with going from State 2 to State3. Since these optics are all in the LVEA area, we expect that the alignment will remain within 10^{-7} rad of the controlled level over reasonably long times scales ($\geq$ 100 seconds).

4.3.3. Recycled MI + one arm locked (state 3)

One of the ETMs is now aligned manually. It is first brought back to the orientation determined during the initial (installation) alignment, by referring to the optical lever and/or suspension sensor signals. If the installation alignment is not good enough that the reflected beam from the ETM falls on the ITM surface, the returning beam will be found in the ITM chamber using the video cameras (see section 5.3.3.) and manual adjustments of the ETM orientation. Once the return beam is on the ITM surface, the ETM orientation will be further adjusted by collapsing the spot pattern as best as possible (using the image from the video camera viewing the ITM surface); at best, this can probably be done such that the ETM orientation is with ~10^{-6} rad of optimal.

At this point the length locking is supposed to proceed to state 3, such that the carrier is locked in the one arm that is now aligned. The interferometer is then more optimally aligned using the relevant wavefront sensor signals, either by manually adjusting mirror angles, or possibly by closing some of the alignment loops.

4.3.4. Full IFO locked (state 4)

The other, until now misaligned ETM is now brought back into rough alignment in the same way as was described for the first ETM. At this point the length locking is supposed to proceed to state 4 - the final state where the full interferometer is resonant. The wavefront sensor alignment loops are then closed (either manually or in response to a trigger from the LSC signaling lock acquisition), followed by the quadrant monitor centering loops.

4.3.5. Alternate procedure

Probably the major weakness in the above scenario is the extremely tight initial alignment tolerance and the potential that a given resonant state is completely disrupted (lock broken) as the new optic is brought into alignment, due to the transient excitation of higher order modes.

An alternative approach which has much appeal is to first lock and align the two arm cavities, in a manner which is at least somewhat immune to the phase conditions in the recycling cavity. Two possibilities are: locking the arm cavities just off their resonant peaks by using the ETM transmitted light power, compared to a measure of the cavity input light power; locking the arm cavities in transmission at their resonances by using a length dither to generate an error signal.

The second method may be difficult (though it was used successfully to lock the first table-top full LIGO-like interferometer in a controlled manner), because the dither frequencies for the two cavities must be widely separated to avoid signal cross-coupling, but also must not be too high above the arm cavity pole frequency to retain a reasonable signal size; these considerations may severely limit the bandwidth of the loops. Advantages of this approach are that the cavities are locked to the center of their resonances, and that the loops can be completely local to the end stations (no information needed from the vertex detectors).

The side-of-fringe locking approach may be more promising, since there is no such bandwidth limitation. The error signal for a cavity would be derived by comparing the cavity's transmitted light with a sample of the light entering the cavity (the recycling cavity pick-off beam). The relative gains of the two channels are adjusted so that a zero error signal occurs when the cavity is slightly off resonance.

5. DETECTION MODE DESIGN

5.1. Advances and Changes

- Wavefront sensor signal modeling: a new sensing matrix was calculated using updated interferometer parameters (as found in the SYS DRD [1]); the wavefront sensing matrix was calculated for the 2 km interferometer (using the parameters found in [1]).
- Wavefront sensor heads (advances and/or changes of the prototype, Fixed-Mass Interferometer sensor): determined the transimpedance (or rf) gain appropriate to the signal levels; selected and tested a 1064 nm-enhanced quadrant photodiode.
- Mode Cleaner alignment control: modeled the wavefront sensor signals from the triangular mode cleaner; identified a sensing strategy using the non-resonant sidebands.
- Servo Modeling: developed a servo model that meets the control requirements in the presence of leaf-spring stacks, high (Louisiana) ground noise, and more above-band filtering; included the effects of the longitudinal (LSC) servo in the model; modeled excitations of the yaw degree-of-freedom using the same basic model as used for pitch
- Quadrant Position Monitors:
- Video Cameras: the design of incorporating local image processing of the video frames has

been discarded, in favor of sending live video from all cameras back to the control room; the number and placement of cameras received further definition.

5.2. Sensor configuration

Fig. 6 shows the functional layout of the ASC sensors. This figure is nearly identical to Figure 11 of the ASC Conceptual Design Document, and is included here for clarity. Compared to the earlier figure, Fig. 6 indicates the feature of the current IOO design that uses the telescope mirrors to control the beam steering into the interferometer.

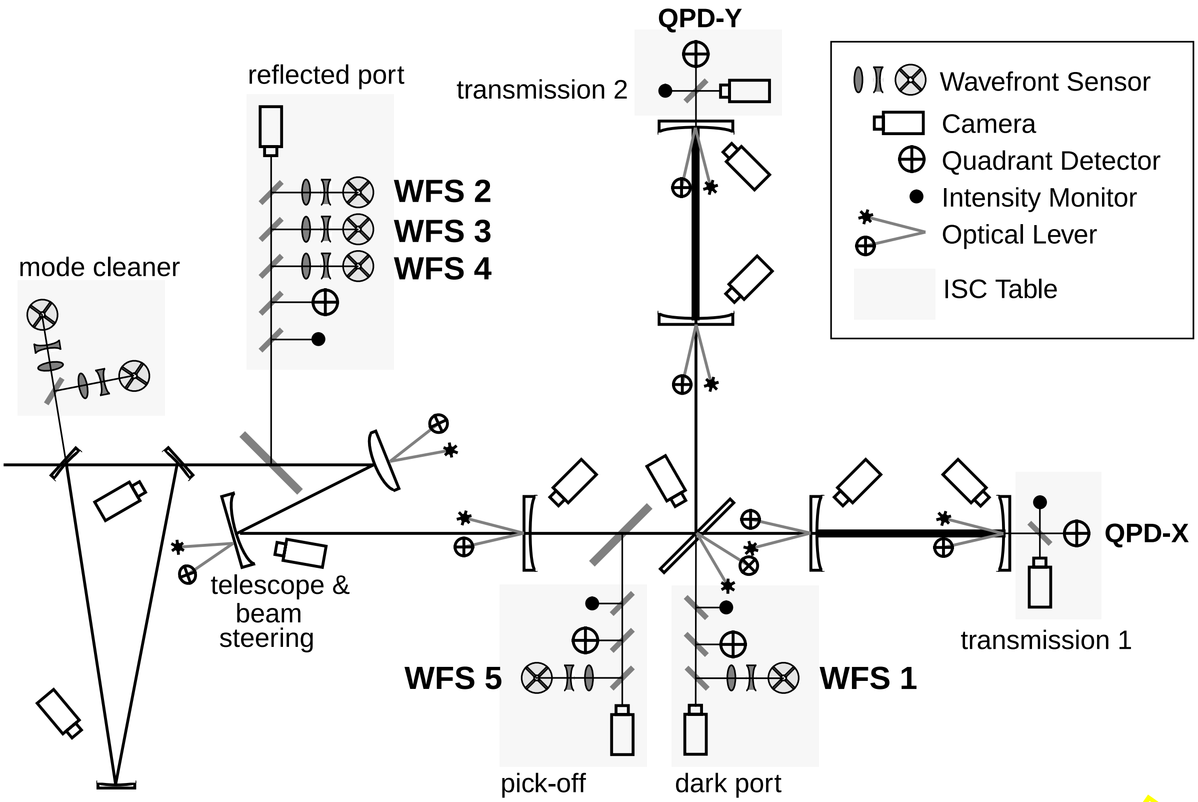

Figure 6 Functional layout of the ASC sensors. The ‘pick-off’ represents a beam from one of the ITM, or the BS, AR surfaces. The ‘symmetric port’ is representative of a sample of the interferometer reflected light. The video cameras which view the chamber interiors are not shown.

An equipment location layout for the ASC hardware is shown in Figure 7. A schematic optical

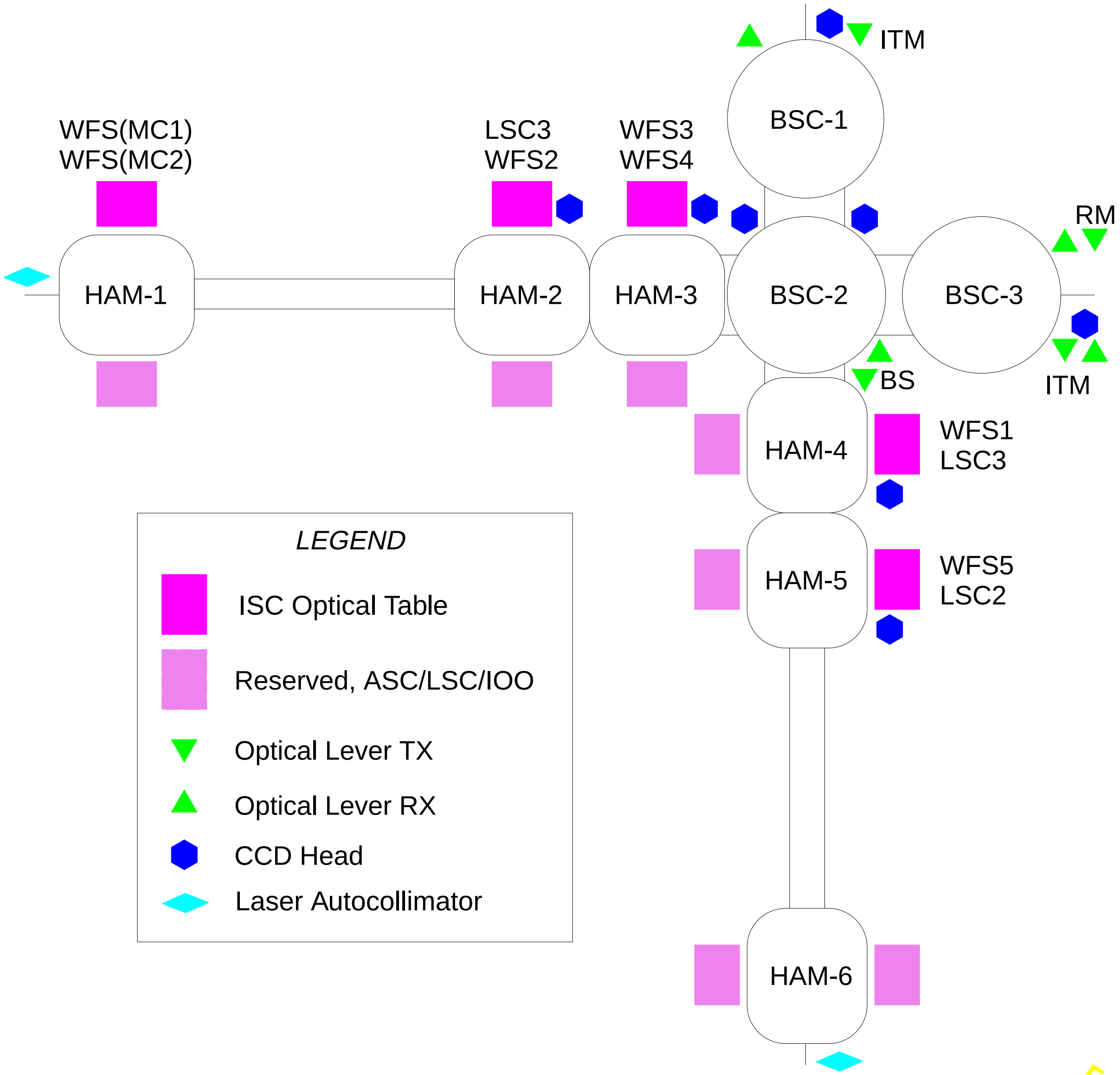

Figure 7 ASC equipment location schematic; vertex station (preliminary)

layout for an ISC optical table is shown in Figure 8.

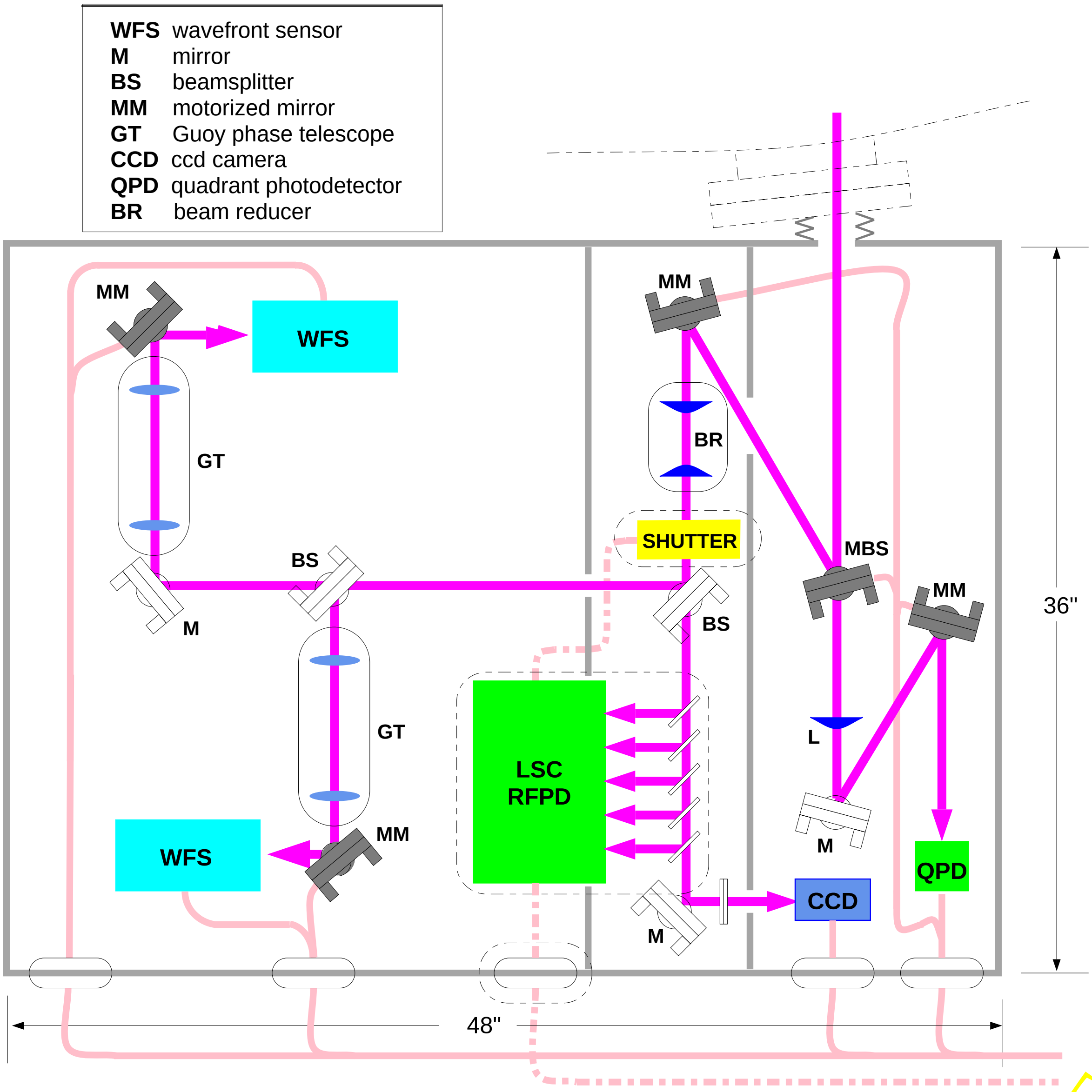

Figure 8 Preliminary ISC optical table component layout. The assembly is shielded by a light-tight safety/dust/thermal enclosure with internal baffles for scattered light control. Bulkhead connectors pass signal and power wiring through the enclosure. The beam entry path from the vacuum port (top) is shielded by a bellows.

5.3. Sensor designs

5.3.1. Wavefront Sensors

At a particular port the wavefront sensor signal in general depends on all five degrees-of-freedom (in one dimension), and it can be written as:

$$WFS(\phi_d, \phi_g, \Theta, \Gamma) = P\, f(\Gamma)\, f_{\mathrm{split}}\, k_{PD}^{10} \sum_{i=1}^{5} A_i \Theta_i \cos(\eta - \eta_{0i}) \cos(\omega_m t - \phi_{0i}) \qquad (1)$$

where for the ith angular d.o.f., Θ_i is the normalized misalignment angle[1], η_{0i} is the Guoy phase at the output port, η the Guoy phase shift added by the WFS telescope, ϕ_{0i} the phase of signal at the modulation frequency ω_m. The coefficient A_i is the rf-modulated component of the optical intensity due to the interference of TEM_{00} and TEM_{10} modes, integrated over a half-plane detector[2]. The units of A_i are watts, and it is normalized to 1 W of total input power; the modulation index is incorporated in the factor $f(\Gamma) \equiv 2 J_0(\Gamma) J_1(\Gamma)$, which for low modulation index reduces to $f(\Gamma) \approx \Gamma$ (A_i is independent of the modulation index). The input power is P, the fraction of a particular port's light that is directed to the wavefront sensor is f_{split}, and k_{PD}^{10} is a less-than-unity factor which

---

[1] Normalized to the beam divergence angle: $\Theta_i = (\pi \omega_0 / \lambda) \theta_i^{\mathrm{real}}$.

[2] A half-plane detector is one that subtracts and integrates over two mirror-symmetric half-infinite planes located left and right of the y-axis.

accounts for the difference between the specific photodiode geometry and the idealized half-plane detector.

	Angular Degree-of-Freedom									
Port	**ΔETM**		**ΔITM**		**$\overline{\text{ETM}}$**		**$\overline{\text{ITM}}$**		**RM**	
Dark	**-25.0**		**-11.4**		-9.9×10^{-6}		-4.5×10^{-6}		1.2×10^{-3}	
	Q	90°	Q	90°	Q	156°	Q	156°	Q	90°
Reflected	2.3×10^{-2}		**-1.37**		-0.73		**6.21**		**-9.60**	
	Q	144°	Q	144°	I	97°	I	146°	I	146°
Recycling cavity	1.84×10^{-3}		**-0.11**		1.43×10^{-2}		**0.52**		**-0.72**	
	Q	144°	Q	144°	I	61°	I	143°	I	144°
Reflected - NR sideband	1.3×10^{-4}		-1.7×10^{-4}		**-2.11**		**-0.965**		**1.93**	
	I	-26°	I	95°	I	90°	I	90°	I	0°

Table 2 Matrix of Wavefront Sensor signals. Top entry in each cell is A_i (with significant values in boldface), lower-left is rf-phase, and lower-right is the Guoy phase.

The matrix of WFS signals generated by the interferometer defined in Table 14 is given in Table 2. In each cell of the table, the top entry is A_i, the lower-left is the rf-phase (I and Q referring to in-phase and quadrature-phase), and the lower-right is the Guoy phase η_{0i} The A_i for the recycling cavity and arm reflection ports include a factor of $3{\times}10^{-4}$, the reflectivity of the ITM AR surfaces.

The splitting factors for the various sensor heads are chosen to make the signal sensitivity (amps of photocurrent per radian of mirror angle) be of the same order of magnitude for all the sensors (this uniform level of sensitivity cannot of course be obtained for both signals - I & Q phase - of sensor 2). This is done so that a common head design (in terms of transimpedance gain and gain range) can be used for all the sensors. This means that we detect relatively less light on the sensors with inherently stronger signals.

The splitting factors and effective optical input power levels for the sensors are shown below.

Wavefront Sensor	*Splitting factor*	*Effective input power, P*	$f(\Gamma)$
WFS 1	0.001	$P_{in} = 6$ W	0.42
WFS 2	0.0024	$P_{in} = 6$ W	0.42
WFS 3	0.02	$J^2_0(0.45) \cdot P_{in} = 5.4$ W	0.05
WFS 4	0.02	$J^2_0(0.45) \cdot P_{in} = 5.4$ W	0.05
WFS 5	0.2	$P_{in} = 6$ W	0.42

5.3.1.1 WFS Error Signal Matrix

The matrix of WFS error signals is now determined by the parameters of Table 2, and the sensors and splitting factors defined above. A remaining parameter in Equation (1) is the photodiode factor k_{PD}^{10}. We take a quadrant photodiode, for which $k_{PD}^{10} = 0.70$; the choice of photodiode geometry is discussed in section 5.3.1.2 below. The other remaining parameters in Equation (1) are the demodulator and Guoy phases. In practice neither phase can be set precisely to the desired value. The assumption is made that the demodulator phase can be set to 1° of the desired phase[1], and that the Guoy phase can be set to 5° of the desired phase. The error signal matrix resulting from these choices is shown in Table 3. The entries correspond to the level of rf-optical power per normalized

---

[1] Each WFS signal will be demodulated in I and Q phase; the resulting demodulated signals will be processed in software to extract the appropriate phase. This is how we believe we can achieve this precision.

angle; multiplying them by the photodiode responsivity gives the actual rf-photocurrent per normalized angle. Any value which was less than 0.01 of the largest value was set to zero.

M_{ij}	***Angular Degree-of-Freedom***					
Wavefront Sensor	**ΔETM**	**ΔITM**	$\overline{\textbf{ETM}}$	$\overline{\textbf{ITM}}$	**RM**	u_i
WFS 1	**-0.044**	**-0.02**	0	0	0	-0.048 u_2
WFS 2a	0	0	-2.0×10^{-3}	**0.026**	**-0.041**	-0.048 u_1
WFS 2b	9.6×10^{-5}	$\mathbf{-5.8 \times 10^{-3}}$	0	4.6×10^{-4}	-7.0×10^{-4}	$(-0.14\, u_1 - 0.40\, u_2 - 0.91\, u_3)(0.006)$
WFS 3	0	0	-7.0×10^{-4}	-3.2×10^{-4}	$\mathbf{7.3 \times 10^{-3}}$	$(0.83\, u_1 + 0.13\, u_4 - 0.54\, u_5)(0.0073)$
WFS 4	0	0	$\mathbf{-8.0 \times 10^{-3}}$	$\mathbf{-3.7 \times 10^{-3}}$	6.4×10^{-4}	$(0.70\, u_1 - 0.46\, u_4 + 0.55\, u_5)(0.0038)$
WFS 5	6.5×10^{-4}	**-0.039**	0	3.2×10^{-3}	-4.4×10^{-3}	$(-0.14\, u_1 - 0.40\, u_2 - 0.91\, u_3)(0.04)$

Table 3 Matrix of misalignment error signals, with the sensor locations and design parameters given in sections 5.2. and 5.3.. Matrix elements are labelled M_{ij}, where *i* refers to the WFS # (1, 2a, 2b, 3, 4, 5) and *j* refers to the angular d.o.f., in the order shown in the table. Units are Watts per normalized angle**.** The u_i are defined in Appendix 1.

5.3.1.2 Wavefront Processing Unit

A block diagram of a wavefront processing unit is shown in Figure 9. The unit includes: the sensor head and Guoy phase telescope, with motorized mirror mount for remote beam centering; the demodulators for the rf-signals; ADCs for the dc and demodulated-rf signals; a signal processing unit; state control outputs and status inputs.

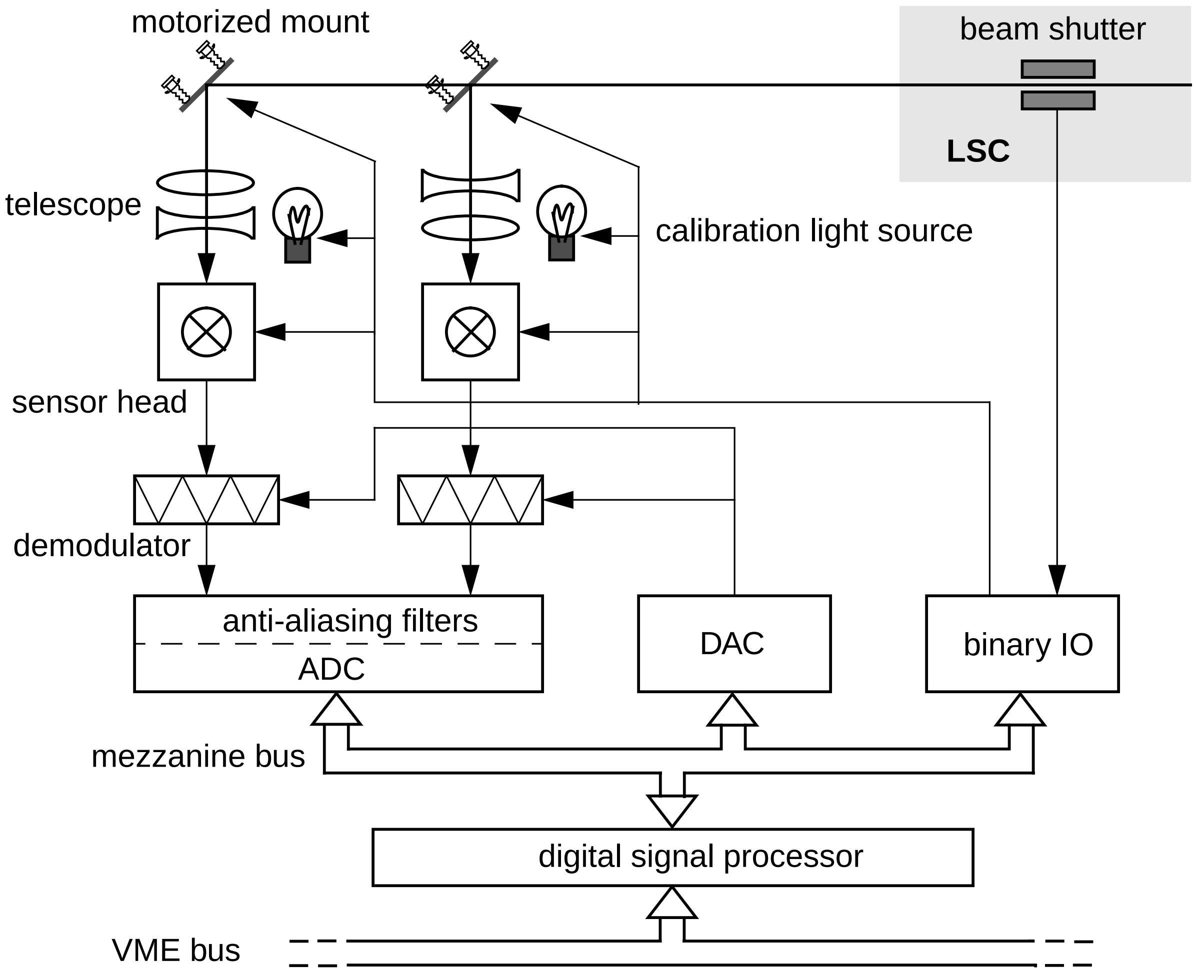

Figure 9 Wavefront Processing Unit (WPU) - more than one sensor head (and associated telescope, demodulator, etc.) may be interfaced to one ADC/signal processing unit. The motorized mirrors are for remote beam centering. The beam shutter sends a status indication to the WPU.

5.3.1.3 Sensor head

The design of the wavefront sensor head and demodulation electronics is based on the prototype wavefront sensors that have been developed for the FMI (Fixed Mass Interferometer) Alignment experiment. This hardware is described in detail in reference [8]. The rf transimpedance gain is different than for the FMI prototype, since the optical gain in LIGO is much larger. The transimpedance is chosen to match the signal levels to the mixer dynamic range - which is 1 V_{pk} at the RF input (1 dB compression point). The rf gain in the sensor head can be changed by a factor of 10;

the high gain is to be used in Detection Mode and the low gain in Acquisition Mode, when larger signals may be present and system noise is less of a concern. In Detection Mode, we are allowing a factor of 10 range between the rms rf signal level and the peak signal level (determined by input range of the mixer).

The angle sensitivity for a given sensor is defined using the root-square-sum of the angle degrees-of-freedom. From the matrix elements given in Table 3, the angle sensitivity at the mixer input in volts/radian per quad element is determined by multiplying by the following factor:

$$(0.45\ \mathrm{A/W})\left(\frac{\text{div angle}}{10^{-5}\,\mathrm{rad}}\right)(10^{4}\,\Omega)\left(\frac{1}{2}\right)\left(\sum_{j} M_{ij}^{2}\right)^{1/2} = 2.25\times10^{8}\left(\sum_{j} M_{ij}^{2}\right)^{1/2}\ \text{volts/rad}$$

The signal levels in the sensor heads are given in Table 4.

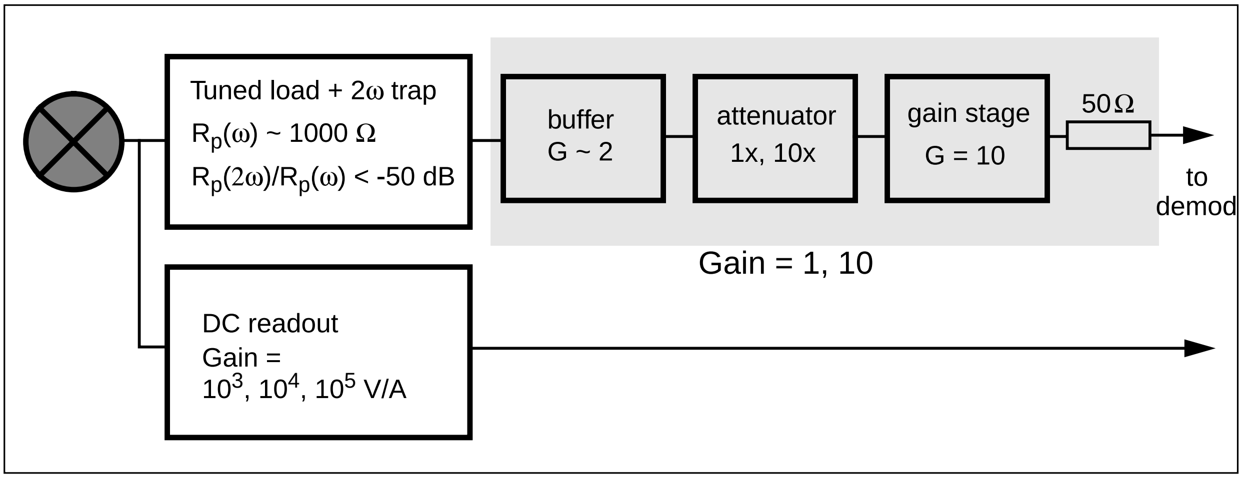

Figure 10 Electronics block diagram of a wavefront sensor head, showing the rf and dc channels for one quad-photodiode element. The blocks within the shaded box show a possible realization of the required gains based on a modification of the prototype WFS heads.

Sensor	*max rms angle, radians*	*rf-diode current, rms*	*mixer rf input, rms*	*Range = (mixer max / rms)*	*rf-diode current, 2ω, pk*	*mixer rf input, 2ω, pk*	*DC diode current*
1	10^{-8}	11 μA	0.11 V	9	55 μA	1.8 mV	64 μA
2	10^{-8}	11 μA	0.11 V	9	25 μA	0.8 mV	50 μA
3	10^{-7}	16 μA	0.16 V	6.25	0.2 mA	6.6 mV	0.4 mA
4	10^{-7}	20 μA	0.2 V	5	0.2 mA	6.6 mV	0.4 mA
5					90 μA	3.0 mV	1.9 mA

Table 4 Signal levels, *per segment of the quadrant photodiode,* for the various sensors in Detection Mode, with a transimpedance gain from photocurrent to mixer input of 10 kohm and a photodiode response of 0.45 A/W.

5.3.1.3.1 Photodiode

The photodiode will be near-infrared enhanced silicon, which typically have a responsivity of ε = 0.45 A/W at 1064 nm. We are currently evaluating the Centronic Inc. model QD50-4X quadrant diode; for this device, we have tested the dark current, capacitance, and series resistance as a function of bias voltage (the capacitance and resistance were measured at 25 MHz). The specifications are given in Table 5. The capacitance and series resistance are compatible with the requirement of a 1 kΩ impedance of the resonant load.

	Dimensions (diam./area per element/sep.) (mm/ mm^2/mm)	*Dark Current*	*Capacitance (pF)*	*Series Resistance*	*Response @ 1064 nm (A/W)*
Manufacturer’s spec.	7.98/50/0.2	150 nA max.	7	not spec’d	0.39 min., 0.47 typ.
Our measurement	—	3.7 μA typ.	5.0	700 Ω typ.	—

Table 5 Specifications for Centronic QD50-4X quadrant photodiode. Capacitance and resistance measured at 25 MHz. Measured dark current is much higher than manufacturer’s spec, but is relatively unimportant to our application.

5.3.1.4 Noise & Error Budget

5.3.1.4.1 GW-band noise

In order that we do not put impractical demands on the above-band filtering, we require that the sensing noise be at least close to shot-noise limited (for post-demodulation frequencies, this applies above 40 Hz). In the case of WFS1 & WFS2, the shot noise is nearly equal to the thermal noise of the resonant tank circuit. We thus require that any electronics noise in subsequent stages does not increase the noise significantly beyond the level given by the sum of the shot noise from WFS1(2) and the tank thermal noise.

Specifically, the noise of the wavefront sensor head must be less than 7 nV/√Hz referred-to-input, or less than 70 nV/rtHz at the mixer input. The demodulator input noise must be less than 20 nV/√Hz, and the ADC input noise must be less than ($G_{if} \cdot$ 50 nV/√Hz), where G_{if} is the value of any post-demodulation gain (used to match the mixer output range to the ADC input range).

The equivalent angle-noise sensitivity, S_{α}, of a given sensor signal can be found by referring the above noise sources to the mixer input, and dividing by the angle sensitivity at the mixer input for that sensor. These numbers are given in Table 6.

WFS	*Angle Sensitivity at mixer input; per element; V/rad*	*WFS head (each channel), at the mixer input; nV/√Hz*		*Demod. input noise*	*ADC input noise[a], nV/√Hz*	*S_{α}, Equivalent angle sensitivity[b], rad/√Hz (f>40 Hz)*
		shot noise	*electronics noise[c]*			
1	1.1×10^{7}	45	70	20	50 *(f>40 Hz)*	9.0×10^{-15}
2a	1.1×10^{7}	40				8.8×10^{-15}
2b	1.1×10^{6}	40				8.8×10^{-14}
3	1.6×10^{6}	115				9.1×10^{-14}
4	2×10^{6}	115				7.3×10^{-14}
5	8.7×10^{6}	250				3.0×10^{-14}

Table 6 Wavefront Sensing Noise

[a] Assuming +-1V ADC range, and referred to input of the pre-ADC whitening filter.

[b] Since two quad elements combine to give one angle signal, the angle sensitivity given here is √2 better than for a single element.

[c] Head noise RTI is thus < 7 nV/√Hz; the thermal noise of the 1kohm resonant circuit is 4.2 nV/√Hz.

5.3.1.4.2 Control-band Noise & Errors

Electronics Noise. In order that electronic noise in the control-band does not limit the residual angle requirement, we require that the base-band electronics noise be less than 100 μV/√Hz in the region f = 0-30 Hz, as referred to the mixer output (or mixer input, assuming a mixer gain of 0 dB). This puts the angle-equivalent integrated-rms electronics noise below 10^{-9} radian for the least sensitive sensors, and below 10^{-10} radian for the most sensitive sensors.

Offsets. A differential dc offset between two opposing channels will, if not measured and corrected for, produce an offset in the controlled angle. Referred to the mixer outputs, the differential dc offsets between opposing channels must be less than 10 mV. This ensures that the equivalent angle offset will be below 3×10^{-9} radian for the least sensitive sensors, and below 5×10^{-10} radian for the most sensitive sensors.

The residual length deviations from resonance can also produce an alignment servo offset since the common mode rejection between opposing channels will not be infinite. However, given the fairly tight residual length requirements, this source of error was shown in the ASC Conceptual Design Document to be, *at worst*, at the 3×10^{-9} radian level (see Table 8 of the Conceptual Design).

Not yet analyzed are errors due to the existence of higher order optical modes (m+n >1) in the system, due to the imperfect optical surfaces.

5.3.1.5 Guoy Phase Telescopes[1]

We have two constraints on the Gaussian beam at the detection plane: first, that its Guoy phase be optimized for maximum detection of the primary degree of freedom, and second, that the spot size be ‘matched’ to the size of the quadrant diode.

The spot size matching results from a trade-off between signal size and centering sensitivity; a smaller spot size implies greater sensitivity to centering errors, whereas a larger spot size is apertured by the photodiode. The dependence of the signal and errors on the spot size and photodiode shape is analyzed in reference [8]. A good solution for a photodiode without a hole is to choose the ratio of beam radius to diode diameter to be roughly 0.2. For the Centronic photodiode, this means a beam size of ω_{det} = 1.6 mm at the detector.

The Gaussian beam at an output port of the interferometer is specified by a state vector

$$\begin{bmatrix} R(z_{port}) \\ w(z_{port}) \\ \eta(z_{port}) \end{bmatrix} \qquad (2)$$

---

[1] This section is derived in large part from reference [10].

where $R(z_{port})$, $w(z_{port})$ and $\eta(z_{port})$ are the wavefront curvature, the spot size and the accumulated Guoy phase shift, respectively; this state vector is determined by the COS beam delivery telescopes. The state vector is then propagated through a a series of lenses and propagation distances to give the desired state vector at the wavefront detector position. Operating on the state vector at the interferometer port with a cascaded series of transformations, we find the focal lengths and positions of the lenses which give the required state vector at the detector.

The Guoy phase at a given detector is chosen to maximize the signal due to misalignment of the primary degree of freedom for which it is responsible For each detector, the magnitude of the off-diagonal terms in the sensitivity matrix have sinusoidal dependence on the Guoy phase shift, but unlike the diagonal terms, they are usually closer to the zero of the sinusoidal variation. The off-diagonal terms of the alignment sensitivity matrix are thus first-order sensitive to the Guoy phase shift, while the diagonal terms are only second-order sensitive. Consequently, some care must be taken in the design and implementation of the Guoy phase telescopes.

Given the uncertainties in the focal lengths and positions of the lenses, an optimization algorithm based on a simulated annealing technique is used to minimize errors in the Guoy phase and spot size, and at the same time make the telescopes as insensitive as possible to uncertainties in their physical layout. We will attempt to use a two lens solution for the telescopes, which greatly simplifies the algorithm for optimizing the design constraints. The typical two-lens design of Guoy phase telescopes that has worked well in the Fixed Mass Interferometer (FMI) is shown in Figure 11. The first lens focuses the beam, more gently for longer focal length lenses. As the beam goes through a waist (near the focal plane), it acquires an additional 180° of Guoy phase. The second lens is placed near the waist formed by the first lens, close to the point where the beam has the desired Guoy phase. Since the spot size near the focus is very small (typically 100 μm), the second lens is usually a strong negative lens which also expands the beam; the beam thus accumulates Guoy phase relatively slowly after the second lens. This is a particularly robust scheme since the distances which are practically most difficult to control are least critical. Specifically, the design is relatively insensitive to the position of the detector, and to the position of the first lens, which is usually a few meters from the output port and can have a large uncertainty. The spacing between the two lenses is crucial, but this is typically a few centimeters and can be determined with high precision.

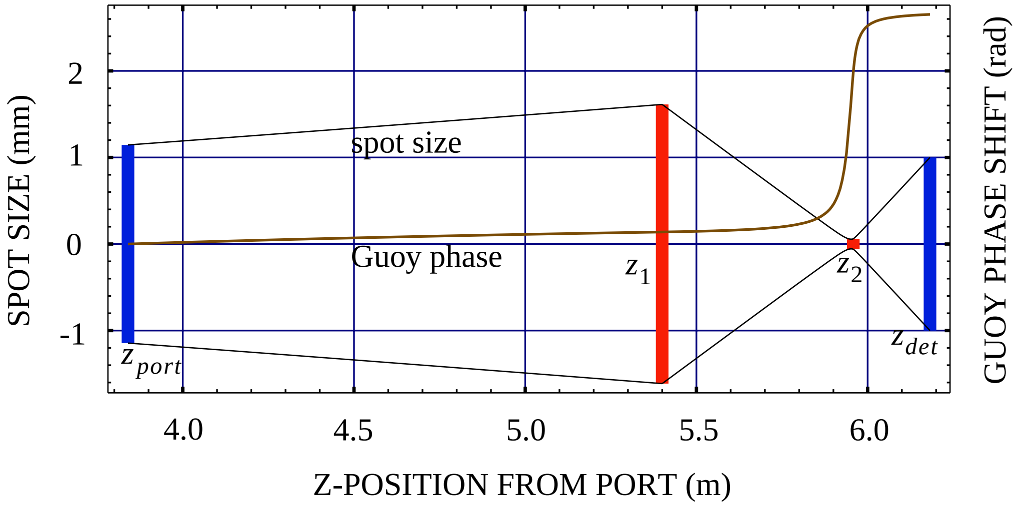

Figure 11 Beam profile and Guoy phase shift for a sample Guoy phase telescope. The spot size and guoy phase shift are plotted as a function of position from the port; z_{port} refers to the position of the port (recycling mirror in this case), z_1 and z_2 to the positions of the first (converging) and second (diverging) lenses, respectively, and z_{det} to the position of the detector.

5.3.2. Quadrant Position Detectors

The quadrant detectors (QPD) at the arm cavity transmission ports are designed to be useful during interferometer acquisition as well as in Detection mode. The conditions and quadrant detector requirements in each mode are given in Table 7.

The photodiodes will be the same as those currently being investigated for use in the wavefront sensors - the Centronic QD50-4X (see Table 5).

When the five wavefront sensor degrees-of-freedom are held to zero, the shift of the beams on the X (on-line) and Y (off-line) arms due to angular deviations of the beamsplitter (BS_{α}) and the input beam (IB_{α}) is given by (in units of fractional shift of the ETM beam per radian of optic angle):

$$\delta_X = 7.8\times10^4 \cdot IB_{\alpha}$$

$$\delta_Y = 7.8\times10^4 \cdot IB_{\alpha} - 1.6\times10^5 \cdot BS_{\alpha}$$

The detection sensitivity of these angles by the QPD's depends on the spot size and photocurrent at the detectors. The parameters are summarized in Table 8.

IFO State	*Power on transmission quad monitor*[a] *(photocurrent per element)*	*Quad Detector Requirements*			
		Transimpedance gain[b]	*Output noise density (f > 30Hz)*	*Output offset drift* [c]	*Bandwidth (3 dB)*
2: Recycled Michelson	3 µW (3 µA)	10 MΩ			> 100 Hz
3: Rec MI + one arm	2 µW / 90 µW (0.2 µA / 9 µA)	10 MΩ/250 kΩ			> 100 Hz
4: Detection Mode	0.1 W (max) (10 mA)	500 Ω	< 20 nV/√Hz	< 5 mV	> 1 kHz

Table 7 Quadrant Position Detector Requirements.

[a] Assuming an ETM transmission of 10 ppm.

[b] Each element; matched to 10V output range

[c] Over the temperature range and time of operation.

Parameter	*QPD-X*	*QPD-Y*
Spot size, radius	1.5 mm	
Photocurrent, per element	4 ma	
Position sensitivity at quad (left-right difference)	15 amp/meter	
Sensitivity to BS, IB angles	1.8×10^3 amp/rad	3.9×10^3 amp/rad
Shot noise	72 pA/√Hz	
Equivalent angle sensitivity	4×10^{-14} rad/√Hz	2×10^{-14} rad/√Hz

Table 8 Signal Detection parameters for the quadrant position detectors.

5.3.3. Video Cameras

The ASC will employ video cameras for two functions, as described below. For both functions, the specific camera and lens types and options will be determined in the final design.

5.3.3.1 Scattered Light Viewing

Video cameras are used to view the vacuum chamber interiors during Initial Alignment, and to monitor the position of the beam on the COC and mode cleaner optics; in both cases scattered

1.06 µm light is collected by the camera's lens. The optic's image on the camera will be determined by periodically illuminating the optic with a light source (external to the vacuum).

A camera and associated hardware is grouped into a Video Camera Unit (see Figure 12). A change from the conceptual design is that there is no local image processing performed. The camera's video output is sent directly to a monitor in the control room. Images from any of the cameras may be 'grabbed' at any time for off-line analysis. The conceptual design indicated that some cameras would have the capability of remote pan, tilt, and zoom functions. We prefer instead to leave these relatively expensive functions off the camera, and instead to increase the number of (relatively inexpensive) cameras in order to ensure the viewing coverage we need; the operator will be able to switch between the various camera signals at a given location to select the desired view. Other options that will possibly be included are a remotely selectable IR filter, and remote focus.

The current design includes 2-4 cameras per BSC chamber for viewing the chamber interior (enough to get adequate coverage; the specific number will be determined during the final design), one camera viewing the (reflective) surface of each core optic, and two cameras to view the surfaces of the mode cleaner mirrors (one for the spherical end mirror, and one for one of the two flat mirrors). Mounting stability requirements for these cameras are not very severe; detailed mounting designs will be developed in the final design, but a likely strategy is to mount each camera to the viewport through which it views (the viewport and mounting hardware are supplied by ASC).

Location	*Number*	*View*
LVEA; at BSC1	2-4	interior of BSC1
LVEA; at BSC2	2-4	interior of BSC2
LVEA; at BSC3	2-4	interior of BSC3
End Station; X Arm/Y Arm	2-4/2-4	interior of BSC9/BSC10
LVEA; at BSC1	1	surface of Y-arm ITM
LVEA; at BSC2	1	surface of beamsplitter
LVEA; at BSC3	1	surface of X-arm ITM
End Station; X Arm/Y Arm	1/1	surface of X-arm/Y-arm ETM
LVEA; at HAM3	1	surface of recycling mirror
LVEA; at HAM2	1	surface of MC mirror
LVEA; at HAM1	1	surface of MC mirror

Table 9 Video Camera locations, number, and viewing function.

Location	*Number*	*View*
ISC Table; Rec Cav sample	1	recycling cavity beam
ISC Table; Anti-symmetric port	1	Anti-symmetric beam
ISC Table; Reflected port	1	Reflected beam
ISC Table; ETM transmission, X/Y Arm	1/1	X/Y Arm ETM transmitted beam
ISC Mode Cleaner Table	1	MC transmitted beam

Table 9 Video Camera locations, number, and viewing function.

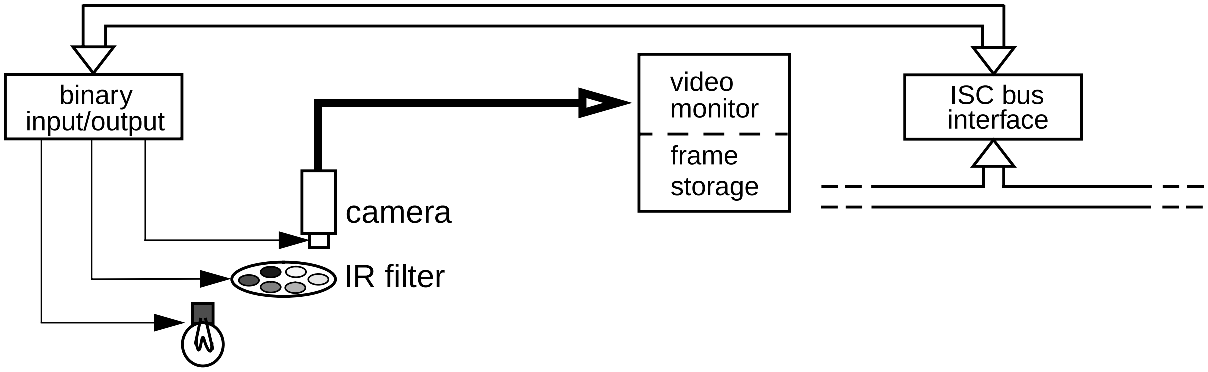

Figure 12 Video Camera Unit.

5.3.3.2 Beam Viewing

Video cameras are also used to detect directly samples of the beam at five locations (as shown in Figure 6): the two ETM transmission beams; the anti-symmetric port beam; the reflected beam; the recycling cavity pick-off beam.

These units of course have no lenses, but probably do include remotely selectable filters. They will be mounted on the ISC optical tables in the LVEA and at the end stations, on adapted, optical lever-type tables.

5.3.4. Optical Levers

In this baseline design, optical levers provide redundant angle readout and an alternate angular error signal source for diagnostics. They also provide for removal and replacement of a critical optic without revisiting the entire initial installation sequence. These roles are less demanding than that originally envisioned (angular control of the interferometer at design sensitivity); in addition, it is now clear that many environmental effects (e.g., the unbalanced vacuum loads on the slab) intrinsically limit the performance of any alignment aid which is referenced to the facility foundations. By setting a drift and repeatability goal of +/- 10 microradians for the optical lever components themselves, we guarantee that the performance will be limited by these external factors. This kind of performance is consistent with that achieved by prototype optical levers in the Caltech and MIT laboratories.

Optical levers are applied to each core optic, plus the final IO output steering mirror. They will use a short lever arm wherever practical, of order 2 to 4 meters. To minimize the effect of intervening optics and air, the transmitter is mounted as close as possible to a viewport giving a direct line of sight to the optic, and the intervening air path is shielded by a flexible seal. The reflected beam may not go directly to an available port; in this case it is redirected by a port-mounted relay periscope (Figure 13).

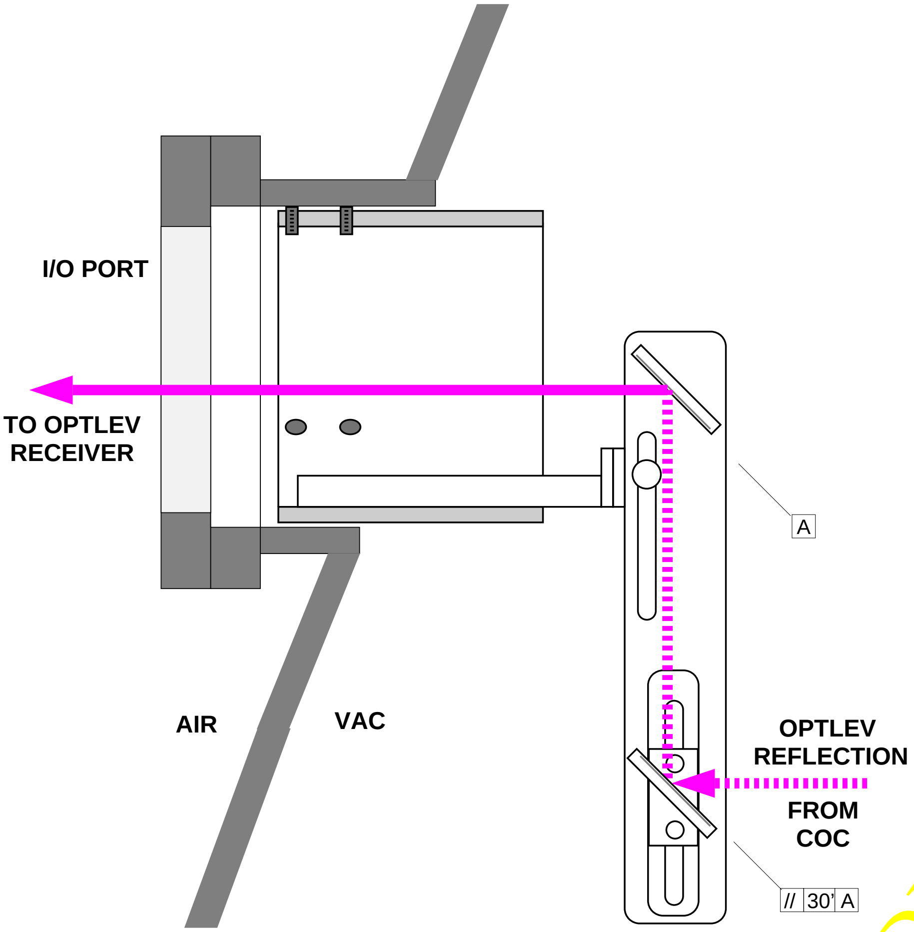

Figure 13 Optical Lever output periscope. Units will permit recovery of optical lever output beams falling within approximately 50 cm of the nearest port, and are field-installable through nozzle with port cover removed.

The optical lever transmitter uses a commercial, fiber-coupled OEM visible diode laser (wavelength 635 - 670 nm) with integral power supply, cooling and intensity control. The laser and power supply may be mounted in the ASC electronic equipment rack, and are joined to a separate unpowered projection optics assembly with a singlemode optical fiber. This projection optics assembly contains a connectorized fiber pigtail with integral GRIN output collimator, which is mounted in alignment with a commercial beam expander. The connectorization permits line replacement of a failed laser or damaged connecting fiber without disturbing preset head alignment. Its output is steered by a motorized mirror (e.g., New Focus Picomotor), which is used to direct the beam onto the mirror inside the chamber. Approximately 2 milliwatts of optical power will be delivered to the vacuum viewport. The entire assembly is shrouded by a removable thermal/dust shield; the air path to the chamber viewport is sealed by a flexible shroud.

The optical lever receiver consists of another motorized beam steering mirror and a quadrant photodetector module. A holder is provided for a fixed optical bandpass and/or neutral density filter in front of the photodetector. In most cases the beam will be matched to the quadrant detector diameter by selection and adjustment of the beam expander, since the lever arms are fairly short compared to the Rayleigh range.

The optics to be controlled will not be optimized for reflectivity at the diode laser wavelength, so we expect between 0.01 and 1 milliwatt to be incident on the receiver's photodetector (a standard Si PIN quadrant diode). The differential current change across the quadrant diode segments corresponding to 10 microradians of optic angle shift will then be approximately 20 nA (assuming a typical lever arm of 2 meters, receiver spot diameter of 5 mm, and photodiode responsivity of 0.3 A/W).

Both transmitter and receiver are supported by pedestals, which are bolted to the facility floor through kinematic intermediate mounting plates. This allows removal and replacement of the pedestal (for example, to access blocked nozzles for chamber entry) without losing alignment references. Stability of these platforms (particularly the transmitter platform) and the transmitter optics assembly is likely to be the limitation to the optical lever's repeatability, and will be investigated experimentally during the final design phase.

5.4. Servo Design

5.4.1. Detection Mode servo

In the preliminary design phase of the servo modeling, two main issues of the servo design were investigated. The first was designing a servo that could meet the control requirements in the presence of a leaf (or coil) spring stack (most of the work for the conceptual design used the viton stack transfer function, and the design did not meet the requirements given the Louisiana ground noise; it now looks more likely that initial LIGO will use leaf or coil spring stacks). The second was to look at the trade-off between servo robustness and more signal filtering above the servo band; this was driven by a desire to simplify the suspension electronics. In addition, the servo model was made more complete by including the effect of the LSC servo which is introducing longitudinal forces to the mirror (previously only the local longitudinal damping loop was included).

5.4.1.1 Control loop design

We found that in order to meet the control requirements on residual angle fluctuations and GW-band noise with the higher Q stack, we had to substantially modify the servo design. A block diagram of the compensation (between the WFS signal and mirror torque control signal) is shown in Figure 14.

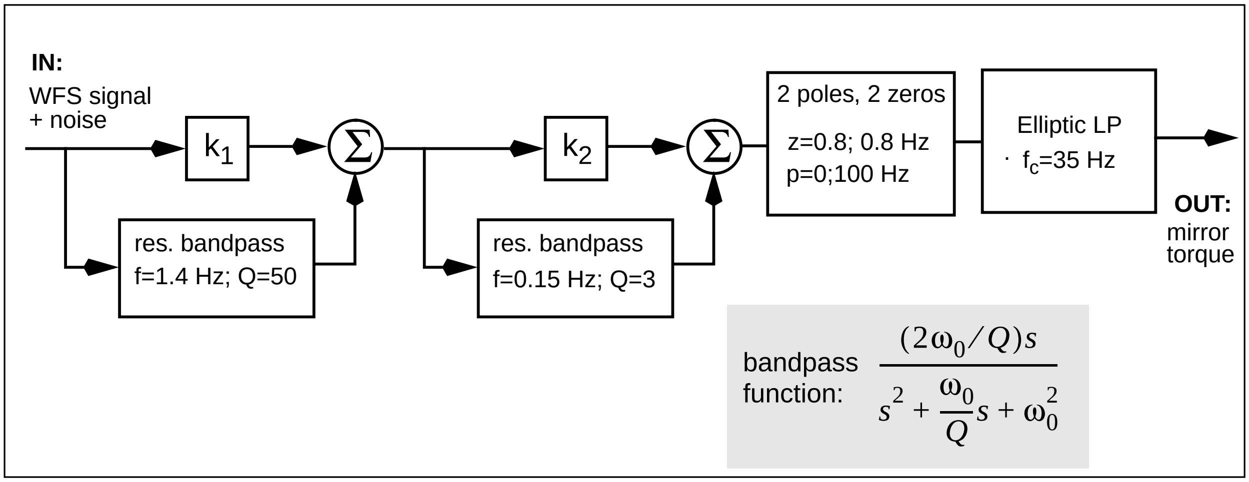

Figure 14 Block diagram of the WFS servo. Several designs of the elliptic low-pass filter were tried; details are given in Table 10 below.

The open loop transfer function of the complete loop is shown in Figure 15.

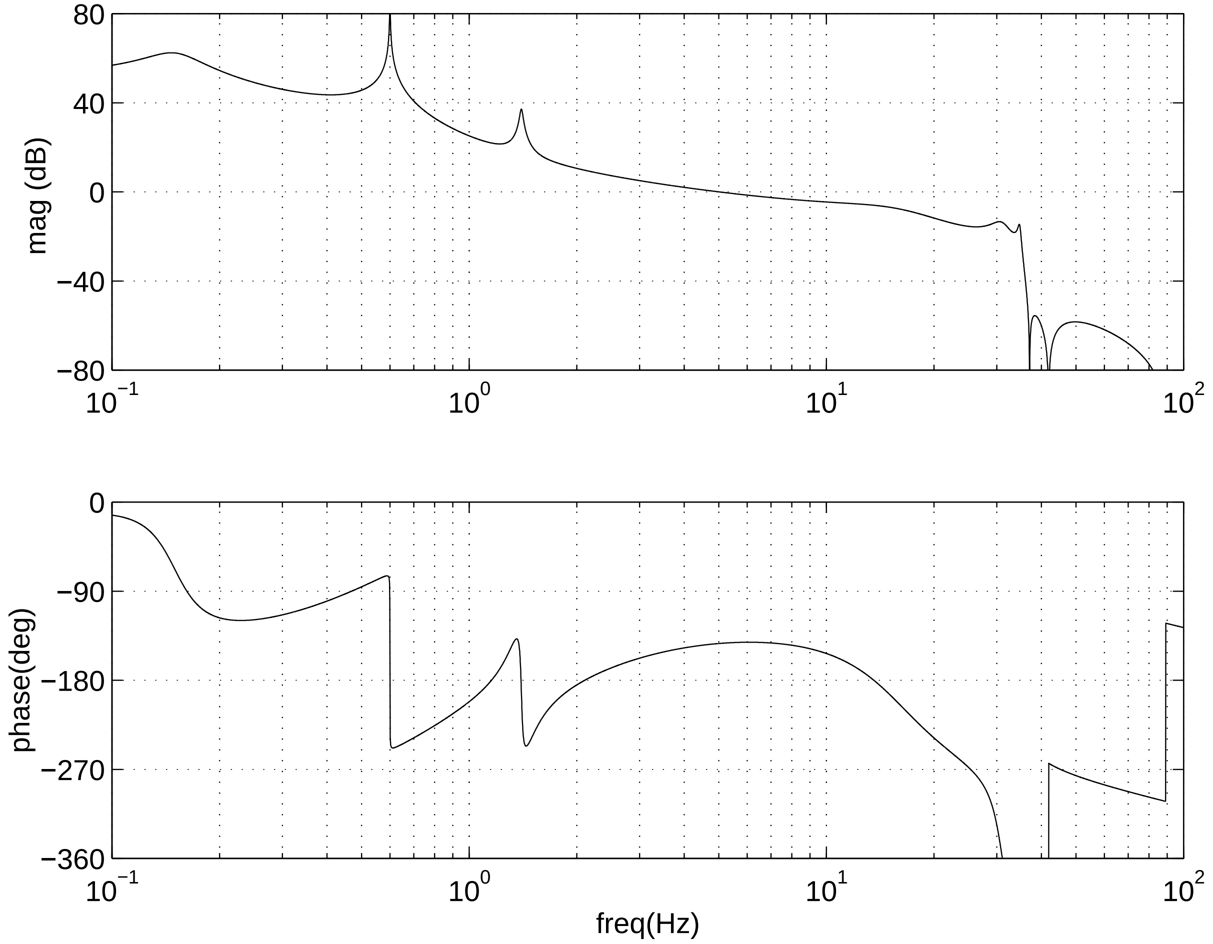

Figure 15 Open loop transfer function of a wavefront sensor control loop. Light damping of the pitch mode at 0.5 Hz is included artificially to limit the response at the resonance. Unity gain frequency is 5.2 Hz; phase margin is 38°.

5.4.1.2 Residual angle fluctuations

The residual angle fluctuations using the above servo in the presence of LA ground noise and leaf spring stacks (refer to reference [7] for details on the ground noise and stacks) is shown in

Figure 16. The elliptic filter design parameters for this simulation were: 6th order, 40 dB stopband attenuation, 4 dB passband ripple. When the model is run using a ground noise time series from Hanford, the residual rms angle (integrated down to 10 mHz) is 2×10^{-9} rad_{rms}.

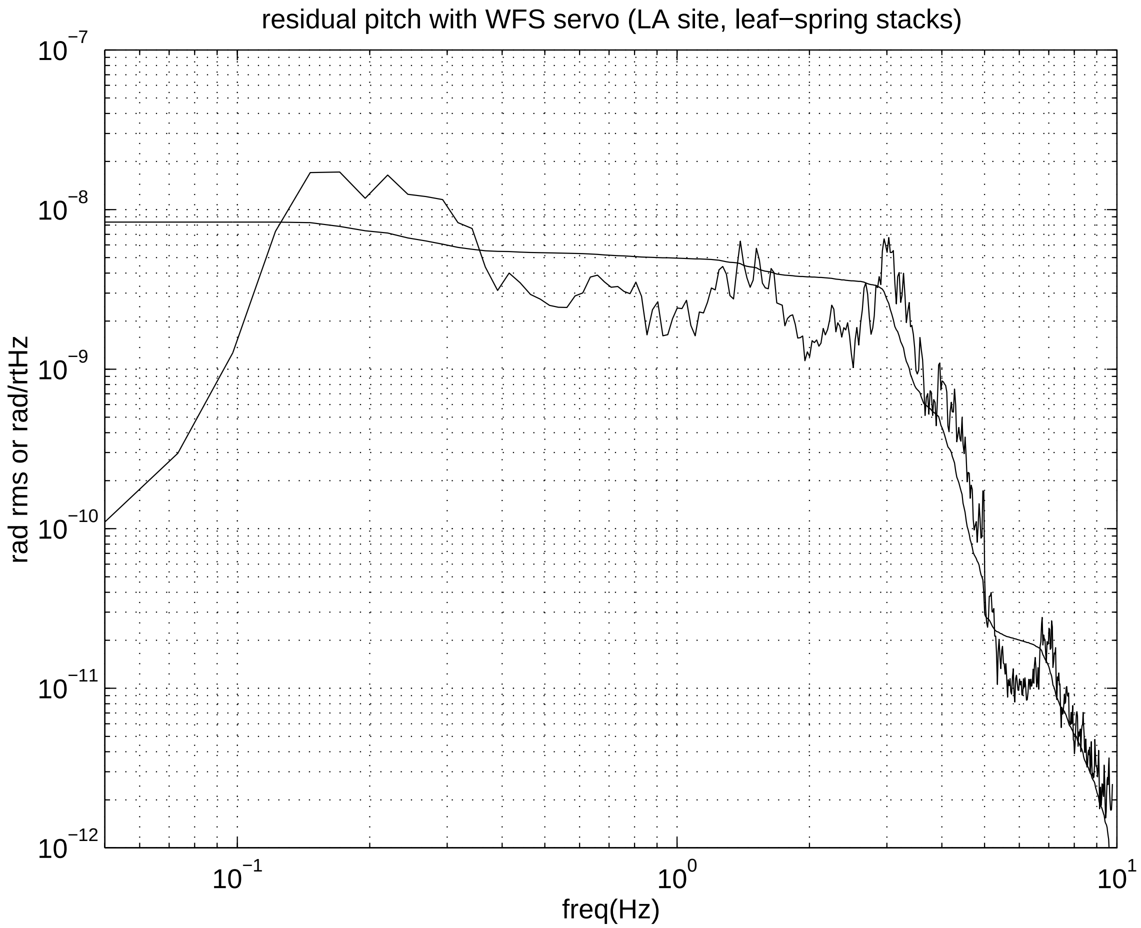

Figure 16 Residual pitch for an optic under wavefront sensor servo control. The smoother line is the rms angle integrated in the band **freq-10 Hz,** and the other line is the spectral density of pitch fluctuations. The integrated rms is below the 10^{-8} rad requirement.

The performance obtained using slightly different parameters for the elliptic low-pass filter is summarized in Table 10.

Filter parameters (stopband atten./ order) f_c= 35 Hz; 4dB passband ripple	*Open loop unity-gain-frequency*	*Phase margin*	*Residual pitch, rms (10^{-8} rad)*	*Freq. at which filter mag. is equal to stopband atten.*
60 dB, 6th order	5.2 Hz	30°	1.05	43 Hz
60 dB, 4th order	6.0 Hz	37°	0.89	70 Hz
40 dB, 6th order	6.1 Hz	38°	0.87	37 Hz
40 dB, 4th order	6.5 Hz	41°	0.81	46 Hz

Table 10 Servo performance summary for different elliptic low-pass filter designs. To speed the design process, the residual pitch was not determined by an explicit simulation, but rather by multiplying input spectra and transfer functions; this overestimates the residual pitch by ~20% (compare the first line in the table to Figure 16).

5.4.1.3 GW-band noise

In the single angular degree-of-freedom model, the mirror angle and displacement noise introduced in the GW-band by the alignment control system is:

$$\theta(f) = S_\alpha \cdot G(f)$$

$$x_m(f) = \varepsilon \cdot S_\alpha \cdot G(f)$$

where S_α is the equivalent angle sensitivity (in the GW-band) of the wavefront sensor channel (see the last column of Table 6), $G(f)$ is the open loop gain, and ε is the angle → displacement cross-coupling in the suspension ($\varepsilon = \Delta x/\Delta\theta$, ratio of unintended displacement to intended angle).

The servo in the preceding section has $G(40\text{ Hz}) = -60$ dB (above 40 Hz the servo gain falls as or more quickly than the noise requirement, so it suffices to show that we meet the requirement at 40 Hz). In order to meet the angular noise requirement, we thus require that $S_\alpha \le 1.5 \times 10^{-14}$ rad/√Hz for $f > 40$ Hz. This inequality holds for WFS signals 1 and 2a; for the other WFS signals, more low-pass filtering is needed, as mentioned in section 5.4.1.5.

Assuming we just meet the angular noise requirement, we then require that $\varepsilon \le 3 \times 10^{-3}$ m/rad. If the cross-coupling comes only from the suspension controllers, this implies that the coil currents must be balanced to 6% or better. The SYS DRD requires the suspensions to be balanced to 1% or better; thus the requirement on the ASC contribution to the displacement noise is met.

5.4.1.4 Effect of LSC servo

Besides dealing with the high Q stack resonance, the current servo design also includes more gain at the microseismic peak - another resonant bandpass section - than the servo in the conceptual design. The need for higher gain at 0.15 Hz became apparent after we added the action of the LSC servo to the longitudinal degree-of-freedom (in the conceptual design, this d.o.f. was velocity damped).

More gain was needed because the mechanical torque on the mirror at low frequencies is higher with the LSC servo than with velocity damping. This is because the angle of the suspension wire - and therefore the torque it produces - depends on the *difference* between the position of the suspension point and the position of the mirror center of mass (CoM). Under local velocity damping, the CoM follows the suspension point pretty closely at the microseismic peak. But the LSC servo holds the mirror's CoM fixed relative to an inertial reference frame; the CoM thus moves with respect to the suspension point with nearly the full microseismic peak amplitude, and the wire torque at this frequency is thus larger than with velocity damping.

The wire torque around the microseismic peak turns out to be about 30× higher with the LSC servo than with velocity damping.[1] The loop gain thus needed to be increased, so that it is at least 10^3 at this frequency; this was accomplished by adding a resonant gain section at 0.15 Hz.

5.4.1.5 Multiple degrees-of-freedom

The modeling in the proceeding sections gives our estimate of the excitations and a servo design for a 'generic' angular pitch degree-of-freedom and wavefront sensor. This should apply well to the critical degrees-of-freedom over the 4 km baseline. Other wavefront sensor signals have less severe residual angle requirements, but poorer equivalent angle noise in the GW-band. The complete multiple-input multiple-output servo modeling has not yet been performed, but in Table 11

---

[1] Since this coupling depends on well controlled mechanical parameters of the suspension, this effect could in principle be made less significant by imbalancing the four coil currents due to the length control signal so as to cancel the wire torque with an opposite coil-magnet torque.

we give the basic servo parameters of the various wavefront sensor signals. The baseline approach to dealing with the multiple degrees-of-freedom is to keep the signals in the wavefront sensor basis for applying the servo functions and some of the low-pass filtering; then the WFS signals are combined to give torque control signals for the individual mirrors, and any LP filtering that is common to all channels is applied before the signals are fed into the suspension controllers. A block diagram of this scheme is shown in Figure 17. We note that though this is the baseline

Sensor	*Sensing direction*	S_α *(rad/√Hz)*	*Filtering req.@40 Hz*	*Target servo BW, Hz*	*Target residual rms angle, rad*	*Mirrors controlled by this sensor*
WFS1	$\mathbf{u_2}$	9×10^{-15}	≥ 56 dB	5	0.8×10^{-8}	All TM’s
WFS2a	$\mathbf{u_1}$	8.8×10^{-15}	≥ 56 dB	5	0.8×10^{-8}	ITM’s, RM
WFS2b	$-.14\mathbf{u_1}-.4\mathbf{u_2}+.9\mathbf{u_3}$	8.8×10^{-14}	≥ 76 dB	2-3	5×10^{-8}	ITM’s
WFS3	$.8\mathbf{u_1}+.13\mathbf{u_4}+.5\mathbf{u_5}$	9.1×10^{-14}	≥ 76 dB	1-2	1×10^{-7}	RM
WFS4	$.7\mathbf{u_1}-.46\mathbf{u_4}+.55\mathbf{u_5}$	7.3×10^{-14}	≥ 76 dB	1-2	1×10^{-7}	All TM’s
QPD-X	**IB**	4×10^{-14}	≥ 70 dB	0.5	2×10^{-7}	IB
QPD-Y	-.9**BS**+.45**IB**	2×10^{-14}	≥ 65 dB	0.5	2×10^{-7}	BS, IB

Table 11 Sensing specifications and nominal servo parameters for each of the sensors used for alignment control. A filtering requirement of X dB means that the open loop gain must be -X dB or smaller at 40 Hz, in order to filter out the sensing noise. In this scheme, four different servo designs are used. The design used for WFS1 and WFS2a is labelled ‘Servo 1’, the design for WFS2b is ‘Servo 2’, the design for WFS3 and WFS4 is ‘Servo 3’, and the design for QPD-X and QPD-Y is ‘Servo 4.’

approach, the electronics will be designed so that any matrix transformation of the alignment sensing signals can be applied (to better diagonalize the signals into some desired basis, e.g.).

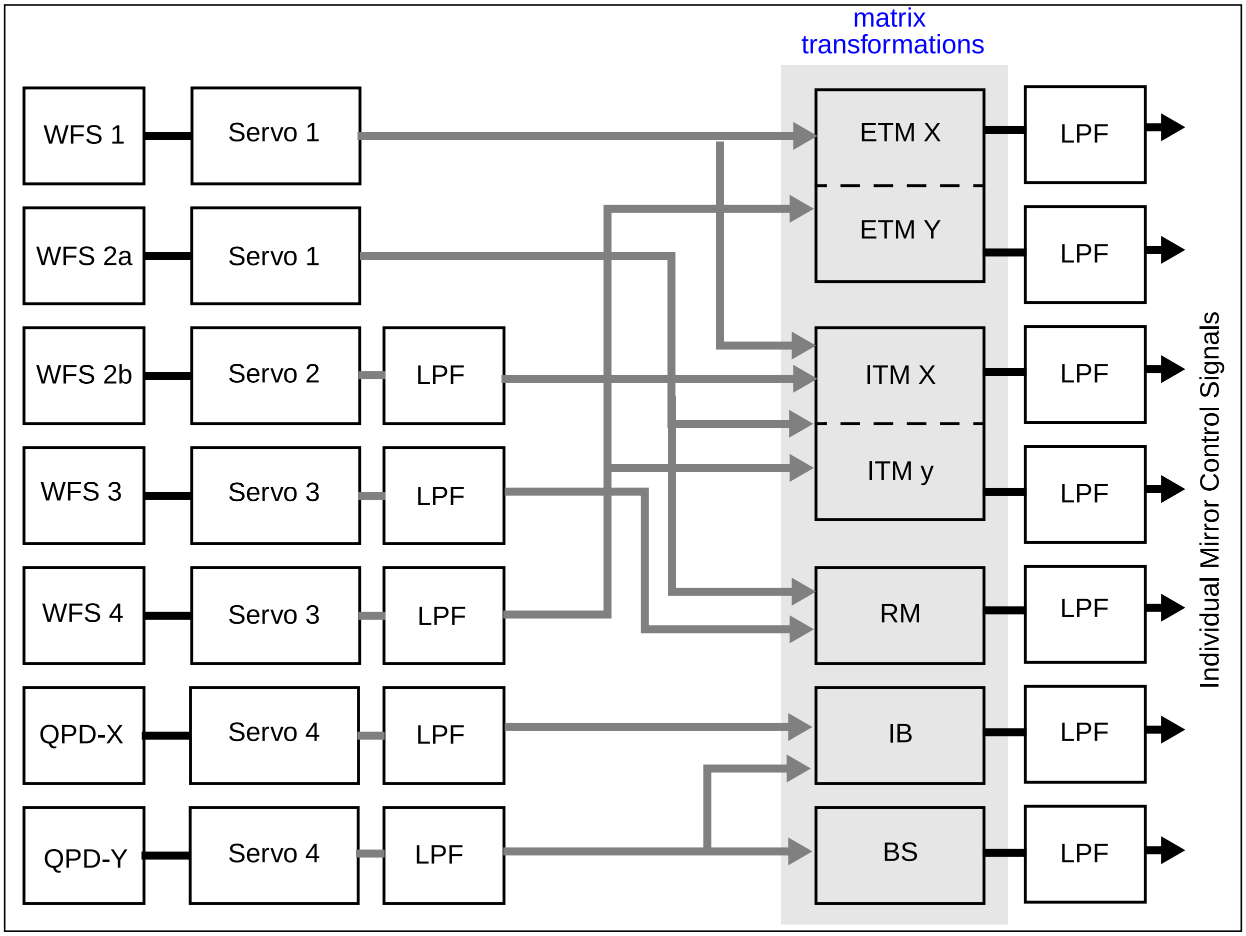

Figure 17 Block diagram of nominal multiple degree-of-freedom servo, where the servo functions are applied in the basis in which the alignment signals are sensed. The final low-pass filter (LPF) is nominally fixed, and supplied as part of the suspension controller. The bottom four channels have additional low-pass filtering (implemented in software) in order to meet the filter requirements given in Table 11. The servo definitions are given in Table 11.

5.4.1.6 Actuation Range & Noise

The DC actuation range for pitch and yaw will be $\pm 10^{-4}$ radians (± 10 divergence angles), for frequencies $f > 10$ mHz. The servo modeling shows that the angular correction in the single degree-of-freedom model is about $\pm 10^{-5}$ rad, dominated by corrections at the microseismic peak (see reference [11]). It is so large due to the length-angle cross-coupling effect described in section 5.4.1.4 above.

For frequencies $f < 10$ mHz, the worst case stack drift in yaw of 8×10^{-10}rad/sec ([12]) determines the range requirement: in order that we have sufficient angular control to maintain alignment over ~10 days, the full suspension angular actuation range of ± 1 mrad is required.

In the GW-band, if the noise everywhere in the loop is dominated by the WFS noise as specified in section 5.3.1.4, the noise at the actuator output will meet the noise requirements for the system. Nonetheless, for clarity we also give the actuator output noise requirements; referred to the noise current in an individual coil channel, the requirements are (assuming the suspension parameters given in reference [13][1]):

- Current noise < 8 pA/√Hz per coil, $f > 40$ Hz.

5.4.1.7 Comparison with requirements

The estimate for the total degradation of the shot noise sensitivity given the performance levels given in the preceding sections is given in Table 12. The requirement is that the degradation be no more than 0.5%, and we see that the estimate is essentially at that level. We note that the residual angle estimates for the dominant degrees-of-freedom correspond to worst case estimates, since they are made under the condition of ‘high Louisiana ground noise.’

Direction	*Residual Angle, radians rms*	*Shot noise sensitivity degradation (%)*
u_1	0.8×10^{-8}	0.21
u_2	0.8×10^{-8}	0.25
u_3	5.5×10^{-8}	0.05
u_4	10^{-8}	<0.01
u_5	1.8×10^{-7}	0.01
	SUM	0.52

Table 12 Residual angles under WFS control. The degrees-of-freedom are assumed to be independent, and the sensor signals are assumed to be stabilized to the degree given in Table 11.

Regarding the control noise requirement, we have not yet made a detailed estimate of the control noise on all the optics, including all the signal channels with their appropriate noise levels and gains (though by following the servo parameters given in Table 11 we should meet the requirements). This estimate will be made as part of the final design, as details of all the loop shapes are developed.

---

[1] Specifically, the DC angle coefficients for the LOS coil-magnet combination are 3.68 mrad/Amp for pitch and 2.55 mrad/Amp for yaw, where ‘Amp’ is the sum of the four coil currents.

5.4.2. Acquisition servo

When we first engage the alignment servos (either in Detection mode or in the acquisition states), we would like a servo loop that is more robust (more gain and phase margin) than the Detection mode servo, but is not restricted by the Detection mode residual angle and noise requirements.

5.5. Mode Cleaner Alignment Design

5.5.1. Initial Alignment

Initial alignment of the mode cleaner is included as part of the interferometer initial alignment task (section 3). This will include setting the optic axis of the MC such that the beam hits each MC mirror within ~2 mm of its center (done be visual inspection of the visible alignment beam), meeting the centering requirement

5.5.2. Alignment Acquisition

The input beam to the mode cleaner must first be aligned well enough so that the MC can be locked on the TEM_{00} mode (input beam angle and position should be within ~1/3 of the MC divergence angle and beam waist, respectively). This will be done by the monitoring spot patterns on the MC mirrors and of the transmitted beam, and manually controlling the input beam direction until the patterns collapse to something close to a TEM_{00} mode. We expect this procedure will need to be done only once at the outset (or if there is a major perturbation to the input beam direction).

The results of modal modeling and prototype experience have both shown that once length control (cavity resonance) is achieved, proper wavefront sensor signals exist for bringing the cavity into optimal alignment. Thus once the MC is resonant, the wavefront sensor loops will be closed.

5.5.3. Detection Mode Alignment

The absolute alignment requirement for the MC is much more tolerant than for the interferometer. The MC beam divergence angle is 200 µrad, and controlling each degree-of-freedom to within 5 µrad of optimal will ensure that the TEM_{00} mode coupling is > 99%.

Wavefront sensors will be used to detect the misalignments of the mode cleaner [T960118-00-D]. The signals will be generated from the interferometer's non-resonant sidebands; they will be detuned slightly from the mode cleaner resonance, so that roughly 10% of the non-resonant sideband power is reflected from the mode cleaner. The non-resonant sidebands will also give a length/frequency error signal that will be used by the LSC to control the mode cleaner length and the laser frequency (both the length and angle signals in this case are a factor of 3 lower than they would be if the sidebands were completely reflected).[1] The advantage of this scheme is that no new sidebands are needed, and that the GW-sensing sidebands are left resonant in the mode cleaner.

The servo system serves to find the optimal alignment and control against drifts; the loop design will have a simple one-pole response, and a maximum bandwidth of 1 Hz. Control may be applied to the either the input beam direction, via steerable mirrors in the IOO (outside the vacuum), or to the mode cleaner mirrors, through the suspension coils; see Figure 18. Ideally we would like to apply the correction to the elements which are drifting more with respect to the telescope and COC optics, but it is not obvious whether this will be the input beam or the mode cleaner mirrors, and we include the option of controlling both in the design.

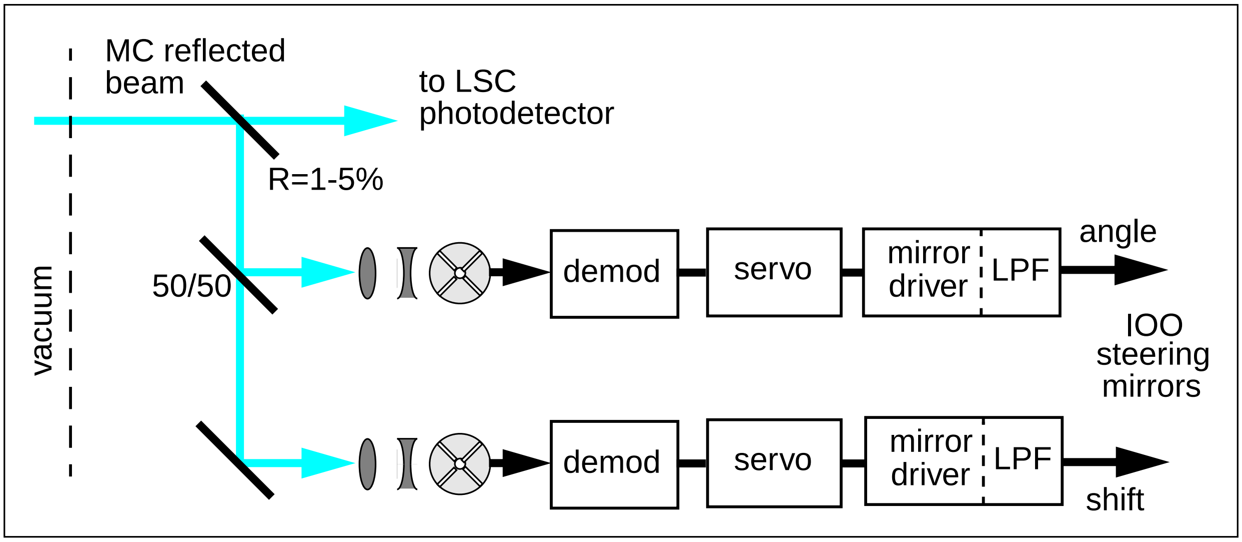

Figure 18 Alignment Control system for the mode cleaner. The low pass filters (LPF) after the mirror drivers serve to filter electronic noise in the GW-band. Alternatively, the control signals may be sent to the mode cleaner mirrors (using different servo compensation).

5.6. 2 km Interferometer

The design of the ASC system for the 2 km interferometer is nominally the same as for the 4 km interferometer. The two additional optics (the folding mirrors) will need to be included in the initial alignment procedure. In Detection mode, the folding mirrors will be locally damped (in angle).

The GW-sensitivity to misalignment, and the wavefront sensor signals for the 2 km interferometer have been calculated and are found in references [4] and [9], respectively. The differences between the 2 km and 4 km systems are small (except for the modulation frequencies); no separate design is needed for the alignment control system of the 2 km interferometer.

---

1. The shot noise limit for the frequency detection using this scheme, assuming a non-resonant sideband modulation index of 0.045, is around 10^{-5} Hz/√Hz, which is more than adequate.

6. TEST PLAN

The Fixed-Mass Interferometer experiment provided successful tests of the wavefront sensing concept applied to a complete interferometer and prototype WFS head and demodulator hardware [10]. In addition a single WFS head and demodulator of the same design have been used to successfully control the differential alignment of the suspended Phase Noise Interferometer. In the future the PNI will be equipped with 3 WFS units, the heads of which will use the specific photodiodes being planned for the LIGO WFS heads.[1]

We are also planning a test of a large subset of LIGO ASC hardware and software in order to prove the validity of the conceptual design, to help with the specifications of the ASC final design and to test the performance of the LIGO ASC electronics (especially aspects of the signal processing and digital control system). Additionally, it will deliver a test setup to check and calibrate ASC hardware before it will be installed into LIGO.

A schematic of the test setup is shown in Figure 19. It consists of one AM laser source, one wavefront sensor, one quadrant photodetector, one suspension, one suspension controller, one optical lever, one camera and one VME system (plus the necessary support equipment). The AM laser light is bounced off the suspended mirror before it hits the wavefront sensor. This makes it possible to digitally close the servo loop between the wavefront sensor and the suspended mirror and to perform a careful bench test of the central pieces of the ASC hardware.

7. DIAGNOSTICS

The ASC diagnostic procedures are divided into internal and external diagnostics: internal diagnostic tests can be performed entirely inside the ASC subsystem, whereas external diagnostic test involve other subsystems as well. External tests in most cases require the interferometer to be operational in a detection-mode-like state. Diagnostic tests on or involving the ASC are outlined in Table 13.

The external diagnostic tests and calibration measurements are initiated by the main supervisory console after the interferometer is in the desired state (see Fig. 20). The ACS/LSC subsystems are then generating the required stimulus to drive mirror angles, mirror positions, etc. Since data from different subsystems have to be analyzed combined, the measured data is — as in the case of the detection mode operation — transferred to the CDS data acquisition system (frame builder) and stored to disk/tape. In order to obtain a self contained data set additional data which might be required to complete the diagnostic analysis, such as the waveform of the stimulus, will be added to the data stream by the subsystems. Consequently, the on-line data analysis software will be used to process the data and to extract the diagnostics and calibration information. In case of a cal-

---

[1] This is a non-trivial point; one of the lessons of the FMI was that the quadrant diodes used there were very unreliable. It will be comforting to have some long term experience with the new diodes.

	Diagnostics	*Type*	*Condition*	*Drive*	*Measurement*	*Monitor*	*Analysis*	*Action*
1	Sensitivity Matrix	external	detection mode	ifo mirror angles sine: 50–200 Hz 10^{-13} to 10^{-12} rad	WFS	SUS sensors opt. lev.	Fourier	update ASC servo matrix & rf phases
2	Centering	external	detection mode	bs & ib direction sine: <1 Hz 10^{-7} to 10^{-6} rad	QMPU bs & ib control	WFS SUS sensors opt. lev.	Fourier	update ASC servo matrix
3	Angle-length coupling	external	detection mode	ifo mirror angles sine: 50–200 Hz 10^{-13} to 10^{-12} rad	LSC signals	WFS SUS sensors opt. lev.	Fourier	adjust transverse mirror positions
4	Input beam jitter coupling	external	detection mode	ib direction sine: 50–200 Hz 10^{-13} to 10^{-12} rad ifo mirror angles static: ~10^{-7} rad	LSC signals (dark port)	WFS SUS sensors opt. lev.	Fourier	update ASC servo offsets
5	Maximum GW sensitivity	external	detection mode	ifo mirror angles static: grid diff. length, e.g. 150 Hz, 10^{-17} m	power LSC signals	WFS SUS sensors opt. lev.	Average Fourier	update ASC servo offsets
6	Mode matching	external	detection mode	mode matching telescope	power	cameras	Average	adjust telescope
7	Frequency response	external	detection mode	ifo mirror angles ib direction step: 1–10 s	WFS angle controls	WFS SUS sensors opt. lev.	Average	update ASC servo bandwidth
8	Transient	external	acquisition mode	seismic	WFS, power LSC signals	SUS sensors opt. lev.	Time series	get smart
9	Photodiode calibration	internal	setup mode	light bulb	WFS (dc & rf)		Fourier	adjust ASC calibration corrections

Table 13 Diagnostic Tests

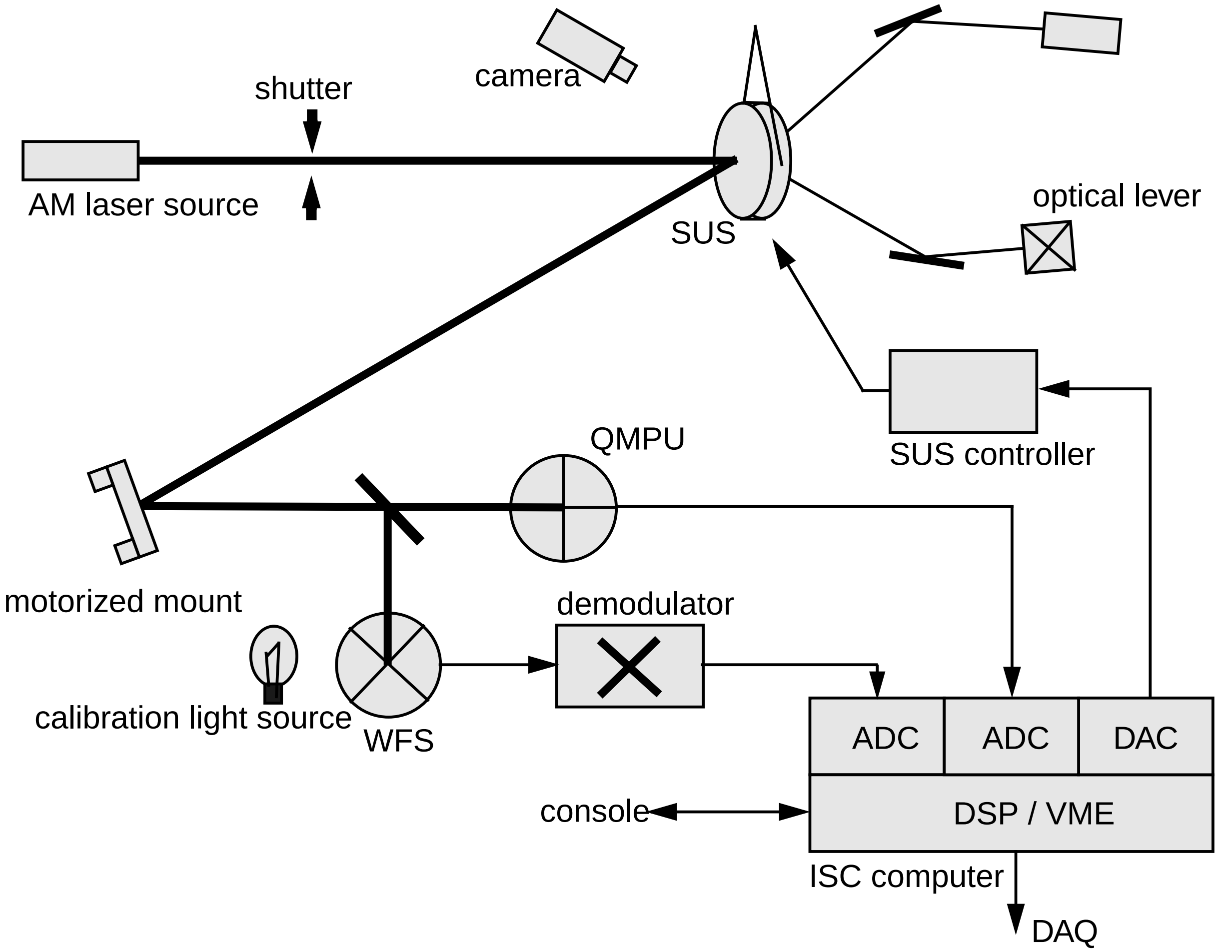

Figure 19 ASC Prototype Setup

ibration run the new calibration data can be used to update the parameters (machine state) of the ASC subsystem.

8. CONCEPTUAL DESIGN OPEN ISSUES

8.1. Sensors for maintaining acquisition alignment

The baseline plan is to use the suspension sensors for this function. However, the design of the optical levers is such that the orientation signals generated from them may be used as inputs to the local angular damping servos if desired.

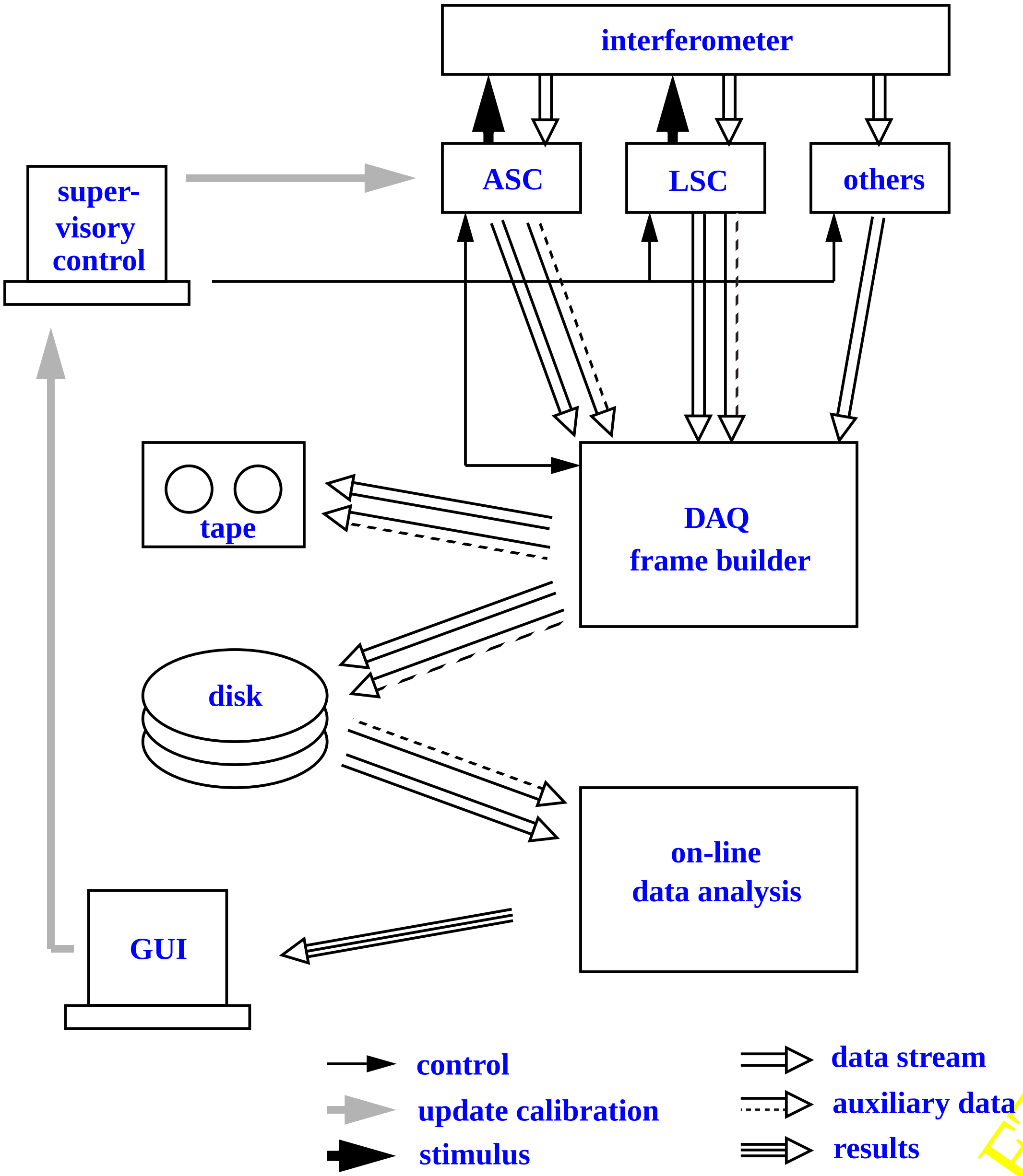

Figure 20 Control and data flow for the external ASC/LSC calibration and diagnostic tests.

8.2. Frequency response of WFS signals

The frequency response of the WFS signals has recently been calculated by Daniel Sigg, by the familiar technique of including audio sidebands into the operators. The results are detailed in reference [14]. As expected, no features in the transfer functions show up until the frequency where the TEM_{10} mode is resonant in the arm cavity, which occurs at 11.4 kHz. We conclude that there is no frequency dependence of the wavefront sensor signals which would be significant for the angular alignment servos.

APPENDIX 1 DEFINITIONS AND PARAMETERS

The interferometer parameters used for the calculations in this document are listed in Table 14, and the properties of the interferometer sensitivity covariance matrix are listed in.

Parameter	Unit	arm (ITM)	arm (ETM)	recycl. (RM)
length (common / differential)	m	3999.01		9.38/0.21
power transmission	%	3	0.0015	2.44
losses	ppm			
radius of curvature	m	-14,571	7400	-9998.65
modulation frequencies	MHz	23.97		35.96 (NR)
modulation depths	Γ	0.45		0.045
wavelength	μm	1.064		

Table 14 Interferometer parameters used in the modeling.

Name	*eigenvector (ellipsoid axis)*					*eigenvalue* σ_i^2
	ΔETM	ΔITM	$\overline{ETM}$	$\overline{ITM}$	RM	
$\mathbf{u_1}$	0	0	0	**-0.58**	**0.81**	-0.00061
$\mathbf{u_2}$	**0.91**	**0.42**	0	0	0	-0.0005
$\mathbf{u_3}$	**-0.42**	**0.91**	0	0	0	-0.116
$\mathbf{u_4}$	0	0	**0.92**	**0.32**	**0.23**	-0.834
$\mathbf{u_5}$	0	0	**0.39**	**-0.75**	**-0.54**	-6.39

Table 15 Covariance Matrix. Eigenvalues (variances) and eigenvectors (axes of direction of variance ellipsoid) of the signal-to-noise matrix.

APPENDIX 2 ASC CHANNEL COUNT

A superset of the ASC channels may be found in an appendix in the ASC Conceptual Design Documentation.

APPENDIX 3 REFERENCES

[1] LIGO-T960112-05-D, *Detector Subsystems Requirements.*

[2] LIGO-T950072-00-R, *Evaluation of proposed changes to the suspension sensor electronics.*

[3] LIGO-T960005-00-R, *Principles of Calculating Alignment Signals in Complex Resonant Optical Interferometers.*

[4] LIGO-T960114-B-D, *Modal Model Update 2, GW Sensitivity to Angular Misalignments.*

[5] LIGO-T960085-00-D, *LSC Configuration Issues*

[6] LIGO-T960065, *Seismic Isolation Design Requirements Document*, section 2.5.5.

[7] LIGO-T960103-00-D, *ASC: Environmental Input to Alignment Noise.*

[8] LIGO-T960111-A-D, *Wavefront Sensor.*

[9] LIGO-T960115-A-D, *Modal Model Update 3, Small Angle Regime.*

[10] *Alignment Issues in Laser Interferometric Gravitational-Wave Detectors*, Nergis Mavalvala, Ph.D. Thesis, M.I.T., January 1997.

[11] LIGO-T97xxxxx, *Comparison of forces and torques from feedback servos for the LSC and ASC.*

[12] LIGO-T960065-02-D, *Seismic Isolation Design Requirements Document.*

[13] LIGO-T960728-00-D, *Requirements of the LOS suspension Driver.*

[14] LIGO-T970058-00-D, *Modal Model Update 7, Angular Transfer Functions.*